REVIEW

Emerging MR methods for improved diagnosis of prostate cancer by multiparametric MRI

Durgesh Kumar Dwivedi[1] · Naranamangalam R. Jagannathan[2,3,4]

Abstract

Current challenges of using serum prostate-specific antigen (PSA) level-based screening, such as the increased false positive rate, inability to detect clinically significant prostate cancer (PCa) with random biopsy, multifocality in PCa, and the molecular heterogeneity of PCa, can be addressed by integrating advanced multiparametric MR imaging (mpMRI) approaches into the diagnostic workup of PCa. The standard method for diagnosing PCa is a transrectal ultrasonography (TRUS)-guided systematic prostate biopsy, but it suffers from sampling errors and frequently fails to detect clinically significant PCa. mpMRI not only increases the detection of clinically significant PCa, but it also helps to reduce unnecessary biopsies because of its high negative predictive value. Furthermore, non-Cartesian image acquisition and compressed sensing have resulted in faster MR acquisition with improved signal-to-noise ratio, which can be used in quantitative MRI methods such as dynamic contrast-enhanced (DCE)-MRI. With the growing emphasis on the role of pre-biopsy mpMRI in the evaluation of PCa, there is an increased demand for innovative MRI methods that can improve PCa grading, detect clinically significant PCa, and biopsy guidance. To meet these demands, in addition to routine T1-weighted, T2-weighted, DCE-MRI, diffusion MRI, and MR spectroscopy, several new MR methods such as restriction spectrum imaging, vascular, extracellular, and restricted diffusion for cytometry in tumors (VERDICT) method, hybrid multi-dimensional MRI, luminal water imaging, and MR fingerprinting have been developed for a better characterization of the disease. Further, with the increasing interest in combining MR data with clinical and genomic data, there is a growing interest in utilizing radiomics and radiogenomics approaches. These big data can also be utilized in the development of computer-aided diagnostic tools, including automatic segmentation and the detection of clinically significant PCa using machine learning methods.

Keywords Prostate cancer · Multiparametric MRI · MR fingerprinting · Restriction spectrum imaging · VERDICT · Computer-aided diagnostic

✉ Durgesh Kumar Dwivedi
   durgeshdwivedi@kgmcindia.edu;
   durgeshdwivedi@gmail.com

✉ Naranamangalam R. Jagannathan
   jagan1954@hotmail.com; nrjgj@yahoo.co.in

1   Department of Radiodiagnosis, King George Medical University, Lucknow, UP 226 003, India

2   Department of Radiology, Chettinad Hospital and Research Institute, Chettinad Academy of Research and Education, Kelambakkam, TN 603 103, India

3   Department of Radiology, Sri Ramachandra Institute of Higher Education and Research, Chennai, TN 600 116, India

4   Department of Electrical Engineering, Indian Institute Technology Madras, Chennai, TN 600 036, India

Introduction

Prostate cancer (PCa) is a common non-cutaneous cancer diagnosed in men and has long been associated with inter- and intra-tumoral heterogeneity [1]. Other issues with the present PCa diagnostic pathway include the risk of overdiagnosis and overtreatment of indolent tumor due to serum prostate-specific antigen (PSA) level-based screening strategy, as well as the possibility of missing a few anterior lesions when using transrectal ultrasound (TRUS) biopsies [2]. Over the past decade, multiparametric MRI (mpMRI) has emerged as an essential technique in the management of PCa. mpMRI is increasingly being used in targeting biopsy, detection, staging of disease, assessment of disease aggressiveness, as a triage test before biopsy, and following up patients after a negative biopsy [3–6].

Prostate mpMRI methods include a combination of anatomic pulse sequences like high-resolution T1- and T2-weighted (T2W)-MRI (multiplanar), and functional MRI pulse sequences such as diffusion weighted imaging (DWI) and dynamic contrast-enhanced (DCE)-MRI [7]. T1W images are used to detect post-biopsy hemorrhage and for evaluation of regional lymph nodes. T2W images are used for zonal anatomy, DWI provides a unique contrast based on differences in the rate of diffusion of water molecules within tissue, and DCE-MRI assesses tumor angiogenesis [8–10]. The current role of DCE-MRI in PCa is debatable, and MR spectroscopic imaging (MRSI), another functional MR tool that measures the concentration of various metabolites is not routinely performed in clinics. The combination of an endo-rectal surface coil and a pelvic phased array coil increases the signal-to-noise ratio (SNR) of MR images. However, due to patient inconvenience, increased cost, time of examination, and limited clinical benefit of the coil at 3 T, the endorectal coil is used only with 1.5 T MRI systems [7, 11].

Despite several advancements in the diagnosis of PCa using MR methods, mpMRI still suffers from high cost, inconsistent image quality, a moderate specificity in the transition zone (TZ) PCa, and inter-observer variability in mpMRI interpretation [12, 13]. As a result of these issues, various groups have been working on developing new MRI methodologies and sequences for improved diagnosis of PCa. In this review, we briefly present the clinical utility of mpMRI in PCa, several novel MR sequences such as advanced diffusion MR-based sequences (restriction spectrum imaging, VERDICT, etc.), perfusion based MR

approach (ASL), luminal water imaging, MR fingerprinting (Fig. 1) as well as various emerging methods for the improved diagnosis and precise decision making in PCa [14].

Current clinical role of mpMRI in PCa

mpMRI in biopsy naïve patients, in targeting biopsy, the diagnosis of clinical significant PCa

The current standard diagnostic pathway for detecting PCa includes abnormal digital rectal exam (DRE) and elevated serum PSA levels. Systematic TRUS biopsies are performed with histological grading based on the Gleason grading system and modifications by the International Society of Urological Pathology (ISUP) to assess the presence of PCa if DRE is abnormal and/or elevated serum PSA levels [1, 2, 12]. A Cochrane review and meta-analysis showed that PSA screening failed to detect a significant reduction in PCa-specific mortality [15]. Thus, there is an urgent clinical need to detect clinically significant PCa (e.g., ISUP ≥ 2 [16] or per PI-RADS v2.1 [7] Gleason score (GS) > 7 (including $3+4$ with a substantial but not dominating Gleason 4 component), and/or volume > 0.5 cc, and/or extraprostatic extension) and to avoid unnecessary biopsies.

mpMRI has the potential to diagnose clinically significant PCa while avoiding unnecessary biopsies. Our group and others have long been using pre-biopsy mpMR-based diagnostic pathway in the management of clinically significant

Fig. 1 A representative example of pulse sequence of MR fingerprinting. **A** A pulse sequence diagram of the magnetic resonance fingerprinting-fast imaging with steady state precession (FISP). A series of FISP acquisitions follows an adiabatic inversion pulse. **B** In the MRF-FISP sequence, a sinusoidal fluctuation of flip angles and repetition periods in a Perlin noise pattern are used. **C**: Each repetition uses one interleaf of a variable density spiral trajectory. To fully sample the centre of the k-space, it takes 24 interleaves, and 48 interleaves for 256×256. At every repetition, the trajectory rotates by 7.5° (reproduced with permission from reference # 14 from John Wiley & Sons from Jiang et al. 2015)
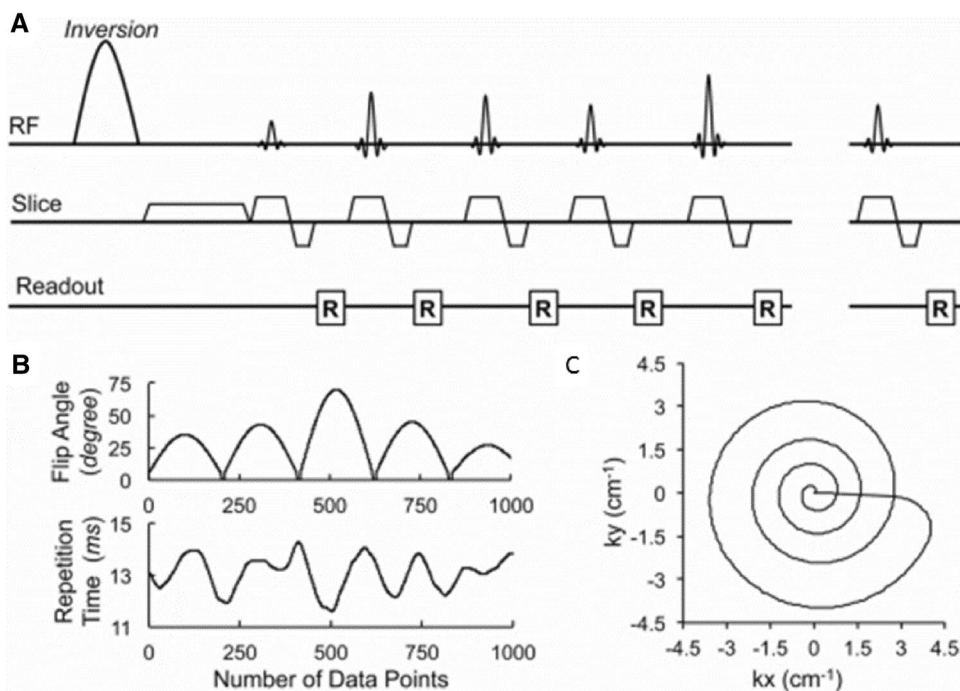
PCa [9, 12, 17–20]. The PROMIS trial, a recent meta-analysis, as well as the MRI-FIRST trial support the claim that MRI has the most favorable diagnostic accuracy in the detection of clinically significant PCa as compared to the standard TRUS-guided biopsy [12, 17–21]. In MRI-FIRST trial, 251 patients were analyzed. This study revealed that 5.2% of patients with clinically significant PCa would have been undetected if systematic biopsy had not been performed, and 7.6% of patients would have been undetected if mpMRI guided biopsies had not been performed [18]. However, in order to reduce costs and scanning time, a few investigators have started evaluating abbreviated biparametric in the detection of the significant cancer as compared with full mpMRI [22, 23]. Moving one step ahead from diagnostic to population-based screening, Evan et al. discussed the challenges of existing screening method and proposed a step-by-step approach of using abbreviated MRI or fast MRI that can be employed as a screening tool for PCa to avoid PSA-level based overdiagnosis of insignificant PCa [24]. Eklund et al. recently conducted a population-based non-inferiority trial of PCa screening using MRI-targeted biopsy to address the problem of overdiagnosis using PSA-based screening [25]. A total of 1532 men with PSA level of ≥ 3 ng/ml were randomly assigned to the standard biopsy group (603 men) and to the experimental biopsy group (929 men). Biparametric MRI (T2W + DWI) were acquired in 846 men in the experimental biopsy group before the biopsy. Clinically significant cancer was found in 21% of men in the experimental biopsy group, compared to 18% of men in the standard biopsy group. It was shown that MRI targeted and standard biopsy performed better than standard biopsy in detecting clinically significant PCa [25].

When working with the large mpMRI datasets of PCa, it is critical to maintain the variability between individual scans performed at different vendor sites to a minimum and provide the highest possible image quality. In order to promote standardized acquisition, interpretation, and reporting of mpMRI of prostate, the PI-RADS was developed. PI-RADS version 2 and more recently version PI-RADS v2.1 have focused on minimizing inter-reader variability and provide technical standards for T2W images and DWI [7, 26]. PI-RADS has improved the sensitivity from 88 to 95% while maintaining specificity for the detection of PCa [27]. The updated version (PI-RADS v2.1) emphasizes a limited role of DCE-MRI, while excluding the role of MRS [7]. Further, to assess the quality of mpMRI scans, the Prostate Imaging Quality (PI-QUAL) scoring systems has recently been developed [28]. Image quality of mpMRI particularly DWI can be improved by using a laxative cleansing enema prior to MR examination [29].

The potential clinical role of mpMRI is in biopsy naïve patient to reduce the number of biopsies in clinically insignificant PCa. Recently, the PRECISION (Prostate Evaluation for Clinically Important Disease: Sampling Using Image Guidance or Not?) trial showed that MRI-targeted biopsy was superior to standard TRUS-guided biopsy in men with elevated serum PSA levels [30]. Another, prospective phase 3 randomized clinical trial showed that the detection rate of PCa ISUP grade 2 or higher was significantly higher in men assigned to MRI and targeted biopsy (38%) than systematic biopsy (26%) in biopsy naïve patients [31]. As mentioned previously, the PROMIS and MRI-FIRST trials demonstrated that mpMRI outperformed routine systematic biopsy in biopsy-naive patients [18, 21]. We developed a risk score and 6-point pre-biopsy mpMRI-based risk calculator as a point-of-care tool to help limit the number of negative biopsies in men with PSA levels between 4 and 10 ng/mL [32]. The developed risk score achieved a higher area under the receiver operating curve (AUC) of 0.87 and found to be highly predictive of PCa. Thus, adopting pre-biopsy mpMRI as a triage test avoids unnecessary biopsies and reduces overdiagnosis of insignificant PCa (Fig. 2) [3, 18, 32, 33].

mpMRI in active surveillance, previous negative biopsy, and abbreviated prostate MRI

mpMRI appears to be a powerful technique in active surveillance for patient selection and the detection of disease progression [34]. Active surveillance is used in patients with low-risk PCa to avoid overtreatment of such patients. Low-risk PCa patients can be routinely monitored using a serial mpMRI and/or mpMRI targeted biopsy. Due to a high negative predictive value of mpMRI, a significant number of patients can avoid unnecessary biopsy. A systematic review and meta-analysis reported a median negative predictive value of 82.4% for any PCa and 88.1% for clinically significant PCa. It was also reported that variation in negative predictive value of mpMRI is due to prevalence, study design, and the definition used for clinically significant disease [35].

Beside these, mpMRI has been shown to be useful in patients who had a previous negative biopsy. A randomized clinical trial showed that MRI-targeted biopsy alone can be used as a method of choice in patients who had elevated PSA and a previous negative TRUS-biopsy [36]. Recently, it has been shown that prostate MRI findings are associated with long-term oncologic outcomes in localized PCa [37]. mpMRI has also shown its utility to select patient for focal therapy which is another treatment option for low- to intermediate-risk PCa. Further, integrating MRI information with clinical and biopsy data may help with tailored patient management [37].

In view of longer acquisition time and limited role of DCE-MRI and MRSI in a full mpMRI protocol, abbreviated biparametric mpMRI have been utilized in the diagnosis of PCa [22, 38]. Kuhl and colleagues evaluated the diagnostic accuracy of abbreviated biparametric prostate MRI in
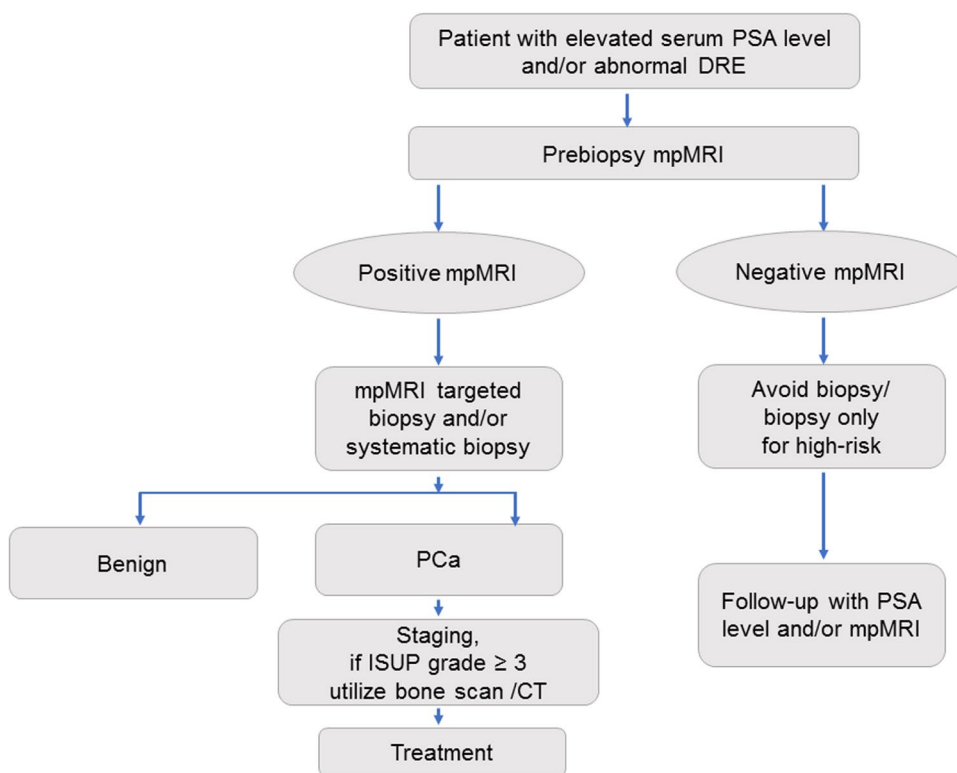
comparison with the full mpMRI protocol in 542 men with elevated PSA level [22]. Biparametric prostate MRI can be acquired faster compared to full mpMRI. Utilizing all of these methods, such as abbreviated MRI and/or full mpMRI, can be used as a triage test in the diagnostic pathway of PCa to avoid unnecessary biopsy and detect the clinically significant PCa. Larger prospective trials are needed to show that an abbreviated MRI is at par with the full mpMRI in the diagnostic pathway of PCa.

Advanced prostate MR sequences

Diffusion imaging methods

Intravoxel incoherent motion (IVIM) and diffusion kurtosis imaging (DKI)

The concept of IVIM was introduced by Le Bihan [39], wherein at least half of the measurements were performed at less than 200 s/mm^2 [8]. It is a potential diffusion modeling technique that utilizes two non-exchanging compartments—vascular (water in the capillaries or blood vessels) and non-vascular (water in and around cells). IVIM model separates the signals from vascular and non-vascular water, such as blood microcirculation in capillary networks providing perfusion value, and measured at low b values (e.g., 0–100 s/mm^2) [26–28]. Although there is

no consensus, on the best processing approach of IVIM data and threshold b value, often it is considered that IVIM effects would disappear for $b > 250$ mm^2/s. Conventionally, the apparent diffusion coefficient (ADC) map can be calculated using a total of three b values, with a low b value of 0–100 s/mm^2, an intermediate b values of 800–1000 s/mm^2, and a higher b value of ≥ 1400 s/mm^2 [7]. Compared to ADC, IVIM can be utilized by acquiring multiple signals at low b values to study a variety of cancer types that showed mixed results [40–42]. Mathematically, it can be expressed as using a bi-exponential model:

$$S(b) = S_0(1 - f)\exp(-bD) + S_0 f\exp[-b(D^* + D)]$$

where b is the strength and timing of the gradients used to generate diffusion-weighted images, S_0 is the signal intensity at $b = 0$ s/mm^2, f is the perfusion fraction and represents the percent of a voxel volume occupied by capillaries, D is the diffusion in the extravascular space, and D^* is the pseudo-diffusion and reflects perfusion in capillaries.

Shinmoto et al. used three orthogonal directions at 10 b values of 0, 10, 20, 30, 50, 80, 100, 200, 400, and 1000 s/mm^2 at 3 T to acquire IVIM-DWI in PCa [43]. Studies show that the IVIM perfusion fractions in malignant and healthy prostate tissues vary, and are not consistent with DCE-derived perfusion parameters [43, 44]. The IVIM model is good in separating signals from vascular water,

but fails to address the microstructure cellular components such as shape, density, and cell size [45].

With advancements in gradient hardware technology, it is possible to acquire DWI at higher b values of up to 3000 s/mm^2 [8]. At high b values ($\geq 1000 - 1500$ s/mm^2), the non-Gaussian diffusion effect predominates due to complex structure of the tissues that provide valuable tissue structure information. Apart from IVIM, non-Gaussian diffusion behavior can also be handled by kurtosis model, bi-exponential model, the stretched exponential model, etc. [8, 46]. Among them, diffusion kurtosis imaging (DKI) and its potential in PCa has been studied by various groups [47, 48]. The ADC derived from the mono-exponential model assumes a Gaussian model, is oversimplified, and provides limited microstructural information. DKI, on the other hand, captures non-Gaussian diffusion behavior and provides tissue heterogeneity [46].

The standard kurtosis model is:

$$S = S_0 \exp[-bD_k + K/6(bD_k)^2]$$

where K is the kurtosis, a dimensionless quantity, and D_k is a kurtosis-adjusted diffusivity.

Wu et al. investigated the utility of DKI in predicting upgrades in GS in 46 patients with biopsy-proven GS 6 [49]. They observed that GS upgrade group had a lower ADC and higher maximum apparent kurtosis coefficient (Kapp)

max and mean Kapp (Kappmean), than the group without an upgrade. Further, Kappmax had the highest AUC (0.82) in upgraded GS [49]. However, a meta-analysis comparing the diagnostic performance of mono-exponential DWI and DKI for PCa found that DKI provides no additional information [50]. Figure 3 shows a representative example of advanced diffusion parameter maps [51]. Feng et al. evaluated the potential of various DW models (mono-exponential, bi-exponential, stretched exponential, and DKI) using 21 b values ranging from 0 to 4500 s/mm^2 with varying averages at 3 T [52]. They found that the mean values of ADC, diffusion parameters of the bi-exponential model $<D>$, f, diffusion coefficient of the stretched exponential model (DDC), water diffusion heterogeneity index (α), and diffusion coefficient of the kurtosis model (Dapp) were significantly lower in cancerous tissues than in benign peripheral zone (PZ) in each group while Kapp was higher in cancer than in benign PZ. However, parameters derived from bi-exponential, stretched-exponential, and kurtosis models did not show superior diagnostic performance than the conventional ADC [52]. A recent meta-analysis reported that various non-Gaussian DWI models (IVIM, bi-exponential, stretched exponential, and DKI) may help detect and characterize PCa but studies with large cohort are required to standardize non-Guassian DWI protocol for improved diagnosis of PCa [47]. Another recent study involving 14 institutions looked at the differences in PCa detection rates using
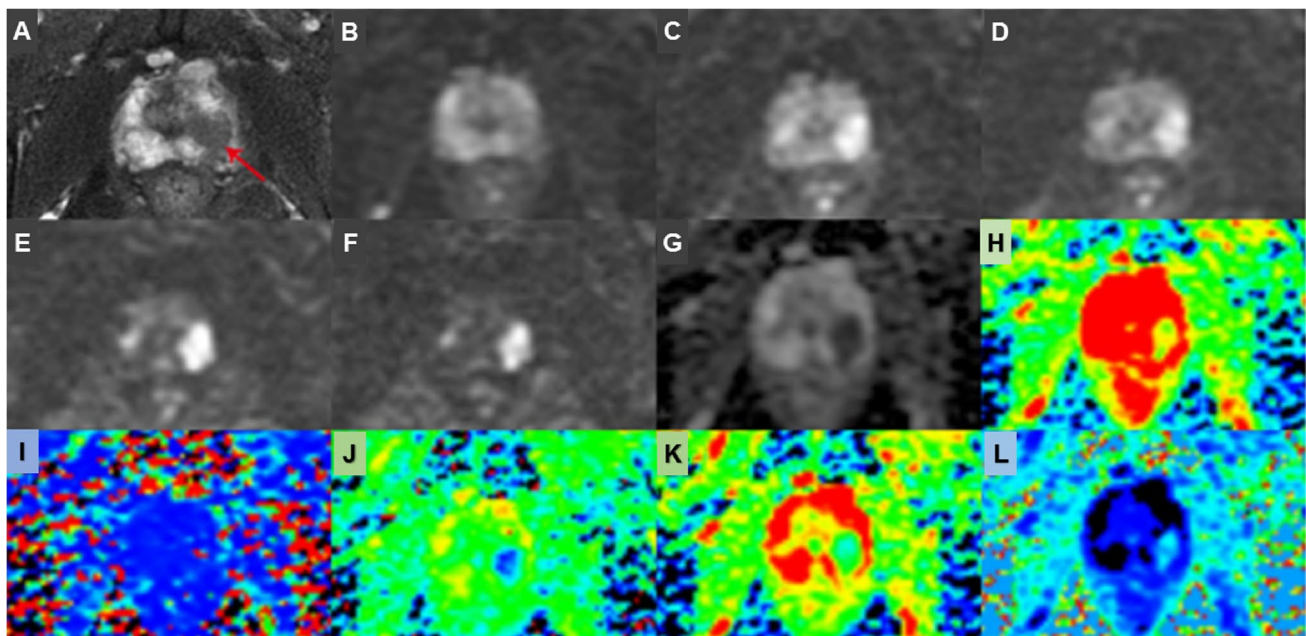

Fig. 3 A representative example of diffusion parameter maps. A 70-year-old man (PSA 7.9 ng/ml) with prostate cancer (GS 4+5=9, lesions in both lobes of prostate, T3a). **A** Lesion on T2WI (arrow); **B**–**F** images acquired with b values of 200, 900, 1100, 2200, and 3000 s/mm^2; as the b value goes up, cancers become more visible; **G** ADC map obtained using a mono-exponential model; **H**–**I** pseudo-color maps of D (0.50×10^{-3} mm^2/s), F (25.45%), D* (8.40×10^{-3} mm^2/s), Dapp (0.94×10^{-3} mm^2/s), Kapp (=0.94) (reproduced with permission from reference # 51 from Springer Nature from Shan et al. 2019)

different DW fitting algorithms (e.g., mono-exponential, bi-exponential, and DK models) [53]. They found a consistent performance of the DW models (mono-exponential and kurtosis fits) in differentiating PCa. Also, it was observed that post-processing decisions might impact the diagnostic accuracy of DWI in PCa.

As mentioned earlier, at low b values IVIM effect predominates while at higher b values kurtosis effect is seen. To estimate both the perfusion and restricted diffusion, Lu et al. developed a hybrid IVIM-DKI model [54]. However, this model suffers from local non-physiological heterogeneity in parameter estimation because of low SNR. To address this issue, Malagi et al. employed an advanced IVIM-DKI to distinguish PCa from benign tumors as an alternative to classic IVIM-DKI model at 1.5 and 3 T [55]. A total of 13 b values (0 to 2000s/mm^2) were used and the data showed high diagnostic performance in cancer detection at 1.5 T, which can be used as an alternative for the traditional IVIM model. Hectors et al. evaluated the potential of conventional mono-exponential DWI, stretched exponential DWI, DKI, and diffusion-tensor imaging (DTI) [56]. They reported that these various diffusion methods have the potential in the detection of PCa [56]. Further larger studies are needed to assess the diagnostic accuracy of advanced IVIM-DKI model in detecting clinical significant PCa.

Nilsson et al. utilized tensor-valued diffusion encoding (b-tensor encoding) in 17 histologically proven PCa [57, 58]. This method provides an estimate of the mean diffusivity (MD), the isotropic kurtosis (MKI), and the anisotropic kurtosis (MKA). An increased MKI was observed in PCa as compared with normal tissue in both the PZ and TZ [57]. Tensor-valued diffusion encoding provided microscopic diffusion anisotropy. Future larger studies related with the b-tensor are needed with an increased in-plane resolution for better accuracy in diagnosing PCa.

Restriction spectrum imaging (RSI)

Among several advanced diffusion-based techniques, RSI, is a DW modeling technique, uses a multishell diffusion acquisition with a range of b values. The RSI can quantify non-Gaussian diffusion in tissue microstructures using a linear mixture model [59–61]. The diffusion signal is generally modeled using several components, such as signal from nuclear volume fraction, cell size, and density, as a function of acquisition parameters such as diffusion time, echo time, and b values. Finally using generalized linear estimates, individual weights are estimated for signals. Since RSI is a multishell acquisition, it can simultaneously acquire geometric information, allowing isotropic and anisotropic orientations to be separated.

In conventional DWI, a combined signal from intracellular (restricted water) and extracellular (hindered),

referred as impeded water, is obtained. However, using compartment filtering and choosing an appropriate diffusion time, RSI enables to get signal from restricted water as the signal from hindered water dissipates quickly. Thus, RSI model includes a spectrum or distribution of hindered and restricted diffusion pools [61].

For prostate RSI, a typical protocol includes b values of 125, 375, and 1000 s/mm^2 with 6, 6, and 15 diffusion gradients, respectively. Also, the acquisition of $b = 0$ images with opposite phase encoding polarizations is used by RSI as a distortion correction method. In PCa, after utilizing multishell acquisition, using geometric filtering it is possible to isolate signal form highly restricted area and isotropic water [62, 63]. In a proof of concept study, this technique was evaluated for the staging of PCa [59]. A total of 27 biopsy proven PCa patients underwent spin echo (SE)–echo planar imaging (EPI)-based RSI prostate MRI along with the standard MRI using an endorectal coil. The range of b values used were 0, 800, 1500, and 4000 s/mm^2 in 30 unique diffusion directions for each nonzero b value. The RSI cellularity maps were reconstructed and standardized with z-score maps. Eight of 9 (89%) patients' demonstrated extra prostatic extension by RSI, while only 22% patients were correctly identified with extra prostatic extension by standard MRI. In another larger study, a total of 100 patients were studied by RSI and mpMRI at 3 T MRI in the same session [63]. The data were compared to the outcomes of a radical prostatectomy or a biopsy. The combination of mpMRI and RSI achieved a higher AUC than mpMRI alone for GS $\geq 4 + 3$. Further RSI performs similar to mpMRI for high grade tumors with the AUC of 0.71 at the sextant level [63]. Felker et al. evaluated the potential of RSI in 189 biopsy naïve men [64]. All patients underwent a pre-biopsy mpMR examination and RSI at 3 T followed by a standard 12-core TRUS-guided biopsy and targeted biopsy using either a cognitive based or fusion based technique. The overall diagnostic accuracies for RSI and DWI were 0.7 and 0.68, respectively. Accuracy of RSI and DWI in PZ was 0.72 and 0.73, respectively ($p = 0.76$), while accuracy of RSI and DWI in TZ was 0.67 and 0.61, respectively ($p = 0.55$) [64].

Besasie et al. assessed mpMRI and RSI to predict Gleason upgrade in 123 men on active surveillance undergoing a repeat biopsy [65]. Overall, RSI increased the AUC from 0.7 to 0.9 to predict Gleason upgrading in men on active surveillance [65]. The RSI technique has several advantages over traditional DWI, such as reduced spatial distortion, improved tumor contrast to noise, and a normalized in vivo assessment of cellularity. One of the drawbacks of RSI is its low SNR. Figure 4 represents a case where RSI outperforms in targeting a biopsy than the standard T2W, DCE-MRI, and conventional DWI techniques [62, 63].
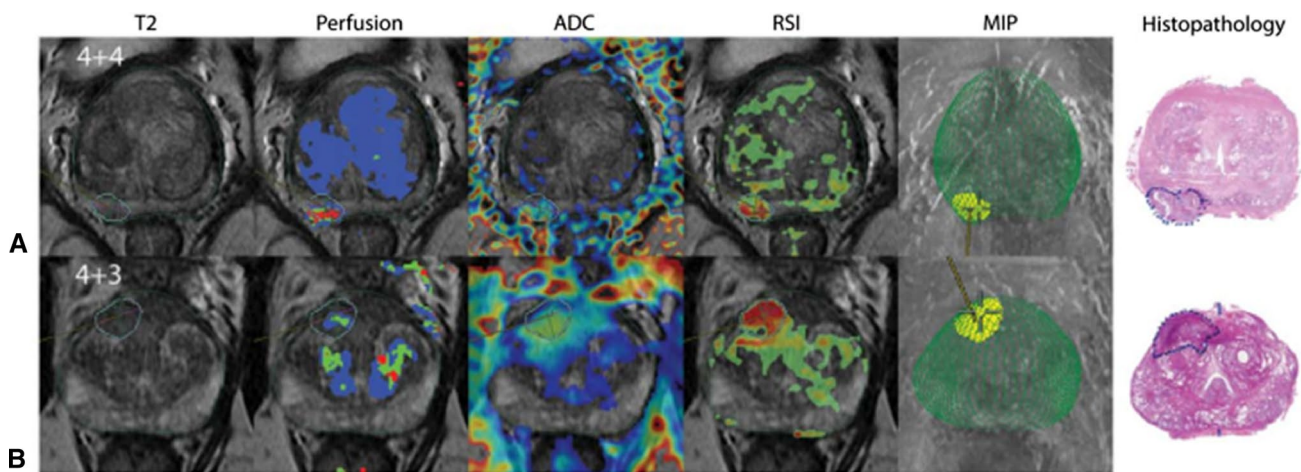
Fig. 4 A representative example of restriction spectrum imaging. **A** An RSI-guided biopsy in which the ADC is equivocal but the RSI clearly identifies the lesion. **B** After a series of negative systematic biopsies, an RSI guided biopsy reveals high-grade PCa. Modified with permission from McCammack et al. PCAN 2016 (reproduced with permission from reference # 62 from John Wiley and Sons from Brunsing et al. 2016)

Vascular, extracellular, and restricted diffusion for cytometry in tumors (VERDICT)

This MR method eliminates the problems of IVIM, while quantifying and mapping histological features [66–68]. VERDICT fits models with various diffusion times and diffusion weightings and assigns the DWI signal to three principal components: (a) intracellular water (S1), (b) water in the extracellular extravascular space (S2), and (c) vascular water in blood in the capillary network (S3) [66]. By using 3-compartment tissue models, VERDICT provides a quantitative detail about cell density, size of cells, intra and extracellular volume fractions.

Mathematically, the VERDICT framework is the sum of 3 compartment models (S1, S2, and S3):

$$S = \sum_{i=1}^{i=3} f_i S_i$$

where S is total MR signal, S_i is the signal from each compartment, and f_i is the proportion of signal with no diffusion weighting from water molecules within the respective population i, $0 \le f_i \le 1$; and the total sum of signal fraction is 1 [66].

VERDICT had previously been validated on colorectal xenograft model and in ex-vivo prostate specimens [66, 68]. A feasibility study was carried out on 8 men with elevated PSA and its performance was compared with ADC, kurtosis, and IVIM [67]. DW images were acquired using single shot EPI and with 9 *b* values (100–3000 s/mm^2).

The model differentiated PCa from benign areas and provided insights on prostate tissue microstructure. Increased intracellular and vascular volume fraction was seen with a decrease in the volume of extracellular–extravascular space in PCa compared with benign regions [67].

A representative example of a patient with GS $3+4$ seen on various parametric maps (the ADC, kurtosis, and VERDICT models) is shown in Fig. 5 [67]. Johnston et al. evaluated the repeatability of intracellular volume fraction maps obtained with VERDICT prostate MRI in 70 men [69]. The intracellular volume fraction map was found to be highly repeatable. Mean intracellular volume fraction was higher in Gleason grade $3+4$ as compared with benign and/or Gleason grade $3+3$ lesions. Interestingly, intracellular volume fraction outperforms ADC in differentiating Gleason grades [69]. VERDICT parametric maps provide information regarding cell size, intracellular volume fraction, extracellular volume fractions, and a pseudo-diffusion coefficient. The VERDICT model does not account for diffusion anisotropy in the prostate and it takes more than 12 min to acquire this sequence.

Zoom DWI and diffusion-weighted whole-body imaging with background body signal suppression (DWIBS)

Routine challenges such as susceptibility artifacts and distortion with conventional single shot EPI-based DWI can be mitigated with 2D selective excitation pulses allowing a focused excitation of reduced field of view [70]. Zoomed DWI improves image quality and reduces image distortion in prostate MRI. Brendle et al. showed that reduced field of view or Zoom DWI provides a better image quality with improved SNR as compared to conventional single shot EPI based DWI [71].
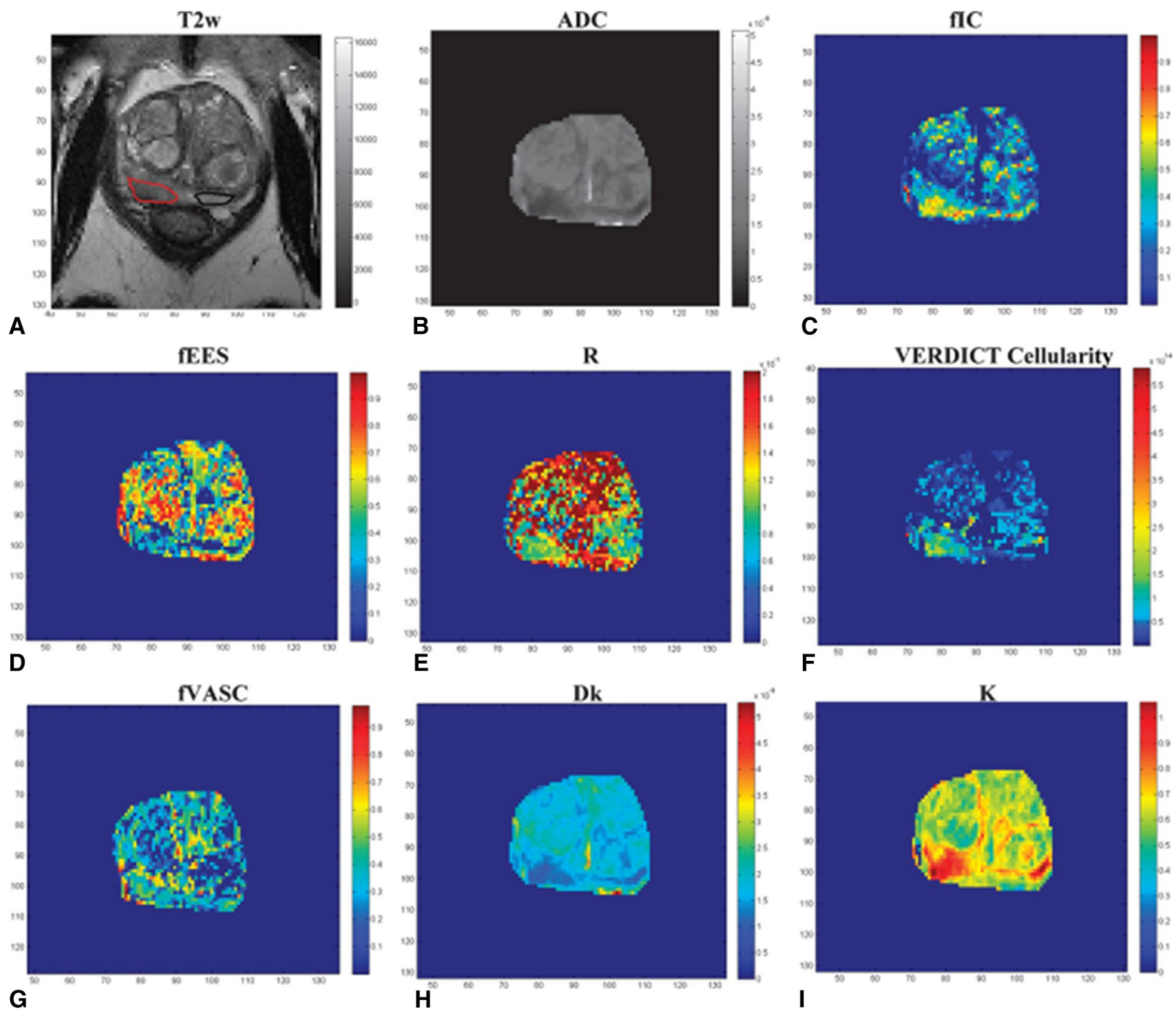
Fig. 5 A representative example of VERDICT and various parameter maps. A 62-year-old man with Gleason score 3 + 4 PZ tumor. The tumour ROI is shown in red, while the benign region is highlighted in black. **A** T2-weighted image; **B** ADC map; **C** volume fraction map of the intracellular compartment; **D** volume fraction map of the extracellular–extravascular space (EES); **E** E, cell radius index map; **F** cellularity map obtained from intracellular volume fraction (fIC) and cell radius (R); **G** volume fraction map of the vascular space; **H** kurtosis diffusivity map; **I** kurtosis map. Unlike the rest of the parametric maps, the cellularity map clearly differentiates the tumor from the benign region (reproduced with permission from reference # 67 from Wolters Kluwer Health, Inc. from Panagiotaki et al. 2015)

Since the 1990s, whole-body MRI has been utilized to study various cancers [72]. Padhani et al. developed a recommendation, the METastasis Reporting, and Data System for PCa (MET-RADS-P), for maintaining quality standards and reporting of whole-body MRI of advanced PCa [73]. DWI is an essential component of whole-body MRI. The concept of DWIBS was introduced by Takahara et al. that provides volumetric DW images of the whole body [74]. Larbi et al. evaluated the potential of whole-body MRI in PCa and multiple myeloma [75]. It was found that any pairwise composition of T1, STIR (short tau inversion recovery), and DWI has a higher diagnostic value to detect bone metastases in PCa. They reported that the pairwise combination of T1-STIR, T1-DWI, and combination of all T1-STIR-DWI provided the highest performance (sensitivity = 100%, 95% CI [90.5–100.0]; specificity = 100% [75.3–100.0]; AUC = 1.00 [0.93–1.00]) for PCa [75]. DWIBS can detect lymph node, malignant skeletal lesions in PCa patients, and provide some incidental findings that may affect the treatment strategy [76]. DWIBS analyzes the entire body and is useful in assessing lymph nodes and distant metastases without using ionizing radiation and the administration of exogenous contrast materials.

Perfusion based MR methods

DCE-MRI

DCE-MRI provides information on tumor vascularity by acquiring series of images utilizing a 3D T1-weighted fast spoiled gradient-echo sequence with a high temporal resolution after injecting the contrast material [77]. Though a higher temporal resolution (~ 5 s) is better, PI-RADS v2.1 suggests to use a temporal resolution of ≤ 15 s with sufficient spatial resolution for DCE-MRI. DCE-MRI is not emphasized in PIRADS v2.1 since it has a limited role in the TZ [7]. DCE-MR images can be analyzed qualitatively, semiquantitatively, and quantitatively [77]. Tumor demonstrates early wash-in and wash-out qualitatively while semiquantitative approach provides various curve parameters (e.g., peak enhancement, time to peak, etc.). The quantitative approach utilizes the Tofts model or the extended Tofts pharmacokinetic modeling and provides various quantitative parameters such as the volume transfer constant (Ktrans), extracellular extravascular volume fraction (ve), and the exchange rate constant (Kep) [78, 79]. However, the semi-quantitative and quantitative DCE-MRI have shown a varying degree of confidence amongst readers thus enabling many to forego DCE-MRI and to use biparametric MRI (T2W and DWI sequences) studies in the evaluation of PCa [80].

Faster sampling and compressed sense methods have improved the quality of MR images and newer DCE-MRI methods that improve the spatiotemporal resolution have been explored [81]. Rosenkrantz et al. investigated a combined approach using golden-angle radial sampling, compressed sensing reconstruction, and parallel imaging (GRASP) for DCE-MRI. Twenty PCa patients were studied using GRASP and standard DCE-MRI methods at 3 T [81]. GRASP provided better lesion conspicuity and structural information and showed improved interreader correlation for lesion size [81].

Another study evaluated the ultrafast DCE-MRI (high temporal resolution ~ 2.2 s) in 20 PCa patients [82]. Signal enhancement and signal washout rate were higher in PCa as compared to normal regions. The AUC for DCE parameters was comparable to ADC and T2 in PZ and the combined T2 + ADC + DCE achieved the highest AUC of 0.92. The downside of this work is that the DCE parameters were obtained using an empirical mathematical model, which cannot be compared to the standard Tofts compartment model [82].

Arterial Spin Labeled (ASL) MRI

ASL measures perfusion level in the tissue without using an exogenous contrast agent and has extensively been used in brain and kidneys [83, 84]. In ASL, protons in the arterial blood are magnetically labeled prior to their entry into the area of interest. Perfusion quantification using ASL can be achieved using various steps, e.g., acquisition of label and control images, reconstruction of perfusion weighted images, and for quantification, modeling the perfusion weighted image signal using a separately acquired proton density image and sequence parameters [83]. ASL labeling can be performed using various methods including pseudo-continuous ASL, pulsed ASL, velocity-selective ASL, vessel-selective ASL, etc.

Li et al. showed the potential of prostate ASL imaging using a modified spatially confined flow-sensitive alternating inversion recovery (FAIR) sequence on 5 healthy subjects [85]. The mean total prostate blood flow was 25.8 ± 7.1 mL/100 cm3/min. Another study reported significantly higher mean blood flow in prostate cancerous areas than benign regions [86]. Further, blood flow measured by ASL significantly correlated with the pharmacokinetic parameters obtained using DCE-MRI in PCa [86]. ASL showed improved contrast ratios both in PZ and TZ in differentiating PCa from benign as compared with signal intensities measured from DCE-MRI [87]. Figure 6 shows a representative example of a biopsy proven PCa patient with increased blood flow measure on ASL [86]. Although ASL does not utilize an exogenous contrast agent, it is intrinsically a lower SNR technique and suffers from susceptibility-induced B0 inhomogeneity [88]. Further studies are required using ASL-based methods to understand PCa angiogenesis.

MR spectroscopy methods

Proton MRS/MRSI

Proton magnetic resonance spectroscopy imaging (^{1}H-MRSI) of the prostate enables non-invasive assessment of various metabolites such as citrate (Cit), choline (Cho), creatine (Cr), and polyamines (PA) [9]. Prostate MRSI (3D chemical shift imaging) is acquired using a point-resolved spectroscopy (PRESS) volume localization method with water and lipid suppression. MRSI of a healthy prostate exhibits a high level of Cit peak at 2.6 ppm, whereas PCa shows decreased Cit with increased Cho (3.2 ppm) due to increased phospholipid cell membrane turnover [89]. Changes in metabolites are quantified by using various metabolite ratios such as Cit/Cho + Cr or Cho + Cr/Cit [9].

MRSI helps to direct targeted biopsies and MRSI-derived parameters, such as metabolite ratios, allow noninvasive
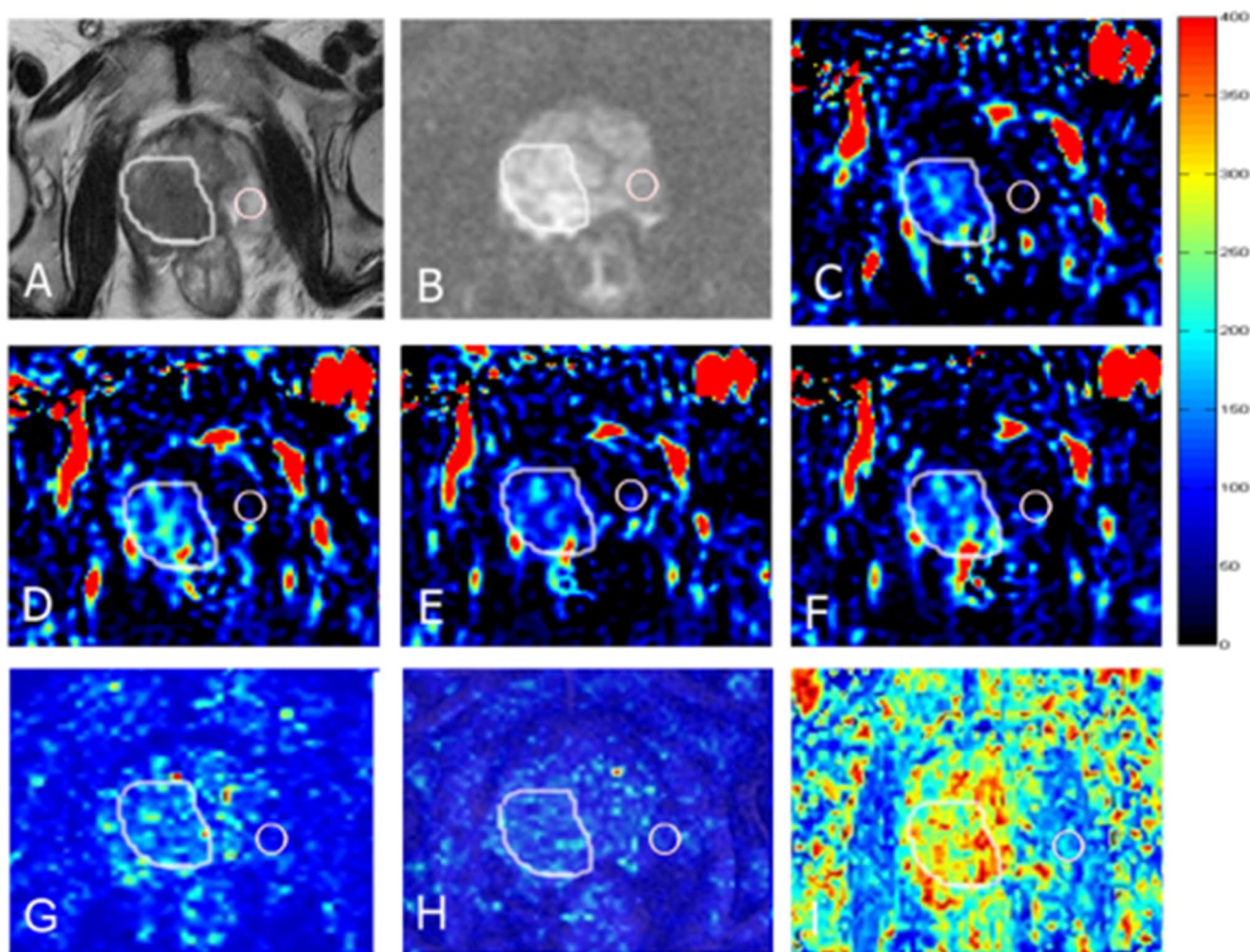
Fig. 6 A representative example of ASL perfusion imaging and quant DCE-MRI maps. **A–B**, A 77-year-old man with PCa in right PZ. The lesion is hypointense on T2-weighted image and hyperintense on diffusion-weighted image; **C–F**, the corresponding blood flow (BF) maps with different T1 values show a higher BF value in the cancerous zone than the benign region; **G–I**, Ktrans, kep, ve maps also show higher values in PCa (reproduced with permission from reference # 86 from John Wiley and Sons from Cai et al. 2014)

assessment of aggressiveness of PCa [3, 20, 90]. A recent meta-analysis showed that MRSI had a pooled sensitivity, specificity, odds ratio, and an AUC of 0.86, 0.78, 22, and 0.89, respectively, in the diagnosis of suspected PCa [91]. Starobinets et al. studied 78 patients using mpMRI (MRSI, DWI, DCE-MRI) prior to radical prostatectomy [92]. Whole mount histopathology was used as a reference in this study. Combination of choline, creatine, and ADC achieved the highest AUC of 1 and 0.99 in distinguishing benign lesions from PCa in the PZ and the TZ, respectively. In the TZ, the combination of Cho and washout slope achieved the highest AUC (0.92) in differentiating $GS \leq 3+4$ from $GS \geq 4+3$. They found that mpMRI can distinguish between benign tissues and PCa both in the PZ and the TZ, as well as mpMRI can stratify aggressiveness of PCa [92].

The majority of earlier spectroscopic studies evaluating PCa utilized PRESS 3D MRSI because of its commercial availability. However, it suffered from long acquisition time and chemical shift displacement error. The recent development of semi-localized adiabatic selective refocusing pulse sequence (sLASER) with gradient-modulated offset-independent adiabatic (GOIA) pulses (GOIA-sLASER) addressed the majority of PRESS 3D MRSI challenges [93]. Gholizadeh et al. evaluated the potential of novel MRSI using a GOIA-sLASER pulses in addition to the routine mpMRI (T2W, DWI, and DCE-MRI) in the TZ PCa [94]. This study also found that the role of DCE-MRI in TZ PCa is limited. The combination of MRSI, T2W, and DWI achieved the highest AUC of 0.99 in the detection of the TZ PCa. Further, metabolite ratio [(Cho + spermine + Cr)/Cit] obtained using the MRSI showed the highest correlation with tumor aggressiveness ($r = 0.64$, $p < 0.01$) [94].

The drawback of traditional PRESS 3D MRSI is a long acquisition time, lipid contamination due to improper water

and lipid suppression, and post-processing of MR spectra. However, it has recently been shown that the new adiabatic pulse-based sequence 3D GOIA-sLASER MRSI is superior to earlier clinically used PRESS 3D MRSI with improved SNR and reduced lipid contamination [93, 95]. As per PIRADS v2.1, MRSI is not currently being used in routine clinical practice [7].

The advancement of 3D GOIA-sLASER MRSI and hyperpolarized ^{13}C-MRI has revived interest in using MRS techniques in PCa [93, 96]. In addition, higher magnetic field strengths, such as 7 T and above, have also demonstrated the potential of MRS due to its improved SNR and spectral resolution [97]. However, both the ^{13}C-MRI and MRS at 7 T still require an endorectal coil which limits clinical applicability and necessitates further technological developments.

Hyperpolarized ^{13}C MRI (HP ^{13}C-MRI)

The low sensitivity of C-13 spectroscopy due to low natural abundance (1.1%) of C-13 isotope can be overcome by the use of C-13 enriched agents and the process of dynamic nuclear polarization. In dynamic nuclear polarization, the dominant hyperpolarization method, the polarization is transferred from electron to the target molecule in a polarizer at a low temperature (approximately 1 K) and at a magnetic field of 3–5 T [98]. HP ^{13}C-MRI magnetizes C-13 probes and provides unique metabolic information relevant to cancer and heart diseases [99, 100].

HP ^{13}C-MRI has shown promising results in preclinical cancer models, in human PCa, and other diseases by providing metabolic information [101, 102]. Dynamic nuclear polarization of ^{13}C-labeled biomolecules (probes) is most widely utilized hyperpolarization method in preclinical research, and currently in human studies. The HP [1-^{13}C] pyruvate is a biomarker used in majority of preclinical cancer investigations. Increased conversion to HP pyruvate to HP lactate has been observed in malignant tissues and this increases with the loss of phosphatase and tensin homolog deleted on chromosome 10 (PTEN) [103]. A recent study included 12 PCa patients who underwent a ^{13}C-MRI using a dual-tuned ^{1}H/^{13}C endorectal coil for signal detection. After injecting [1-^{13}C] pyruvate, HP carbon-13 spectra were acquired using a 2D dynamic echo-planar spectroscopic imaging (EPSI) sequence [103]. It was observed that hyperpolarized lactate increased with Gleason grade. Further, RNA sequencing data revealed that regions of high HP lactate were associated with elevated monocarboxylate transporter 1. This seminal study established a relationship between metabolic information obtained from HP pyruvate MRI and genomic alterations, showing the potential of HP-MRI in understanding cancer biology and assessing therapy response [103]. HP ^{13}C-MRI is an emerging molecular imaging method that can assess pathway-specific

metabolic alterations. A current limitation of HP ^{13}C-MRI is the complexity of the technique. Also, HP ^{13}C-MRI-related studies are limited to a few institutions; therefore, a multi-institutional larger study is needed to evaluate the role of HP ^{13}C-MRI in the diagnosis of PCa.

Other advanced MR methods

T2 maps and luminal water imaging (LWI)

T2 maps can be generated after acquiring several T2W images at different echo times. Quantitative T2 maps can be useful in dealing with the subjective aspect of T2W [104–106]. Quantitative T2 map is acquired using a traditional multi-echo spin-echo sequence with increase in echo times or through accelerated T2 relaxometry [106, 107].

T2 of normal PZ is 122.2 ± 33.8 ms and in the central gland the value is 88.2 ± 13.3 ms [108]. T2 map showed a higher positive predictive value compared to standard T2W images [104]. The highest AUC was achieved using quantitative T2 values in differentiating PCa and normal gland tissue as compared with ADC [106]. Sixteen individuals were studied using a 32-echo spin-echo procedure to evaluate multi-exponential T2 decay in prostate tissue, which demonstrated bi-exponential T2 decay, indicating slow or no water exchange between contributing tissue components [109].

Sabouri et al. developed LWI using three-dimensional multiecho spin-echo where a total of 64 echoes were acquired [110]. The signal decays were fitted to a multi-exponential function (using a regularized non-negative least squares) to measure various T2 components. Using this method, luminal water fraction (LWF) can be quantified which represents the fractional volume of the luminal space [110]. It was observed that PCa had a lower LWF as compared to normal and benign prostatic tissues [110]. Devine et al. correlated LWI with the VERDICT model and observed that LWI alone can predict PI-RADS v2 score groupings with a comparable AUC to that of ADC. Further, LWI parameters correlated with the VERDICT parameters, suggesting that LWI is sensitive to the underlying tissue microstructure [111]. LWI is sensitive to the tissue microstructure, where the stroma and epithelium constitute a short T2 component, while the lumen constitutes a long T2 component. However, most prior studies on LWI were conducted in a small cohort, a larger clinical trial will help include LWI into mpMRI. Figure 7 shows a representative example of MR parametric map for LWI [110].

Hybrid multi-dimensional MRI (HM-MRI)

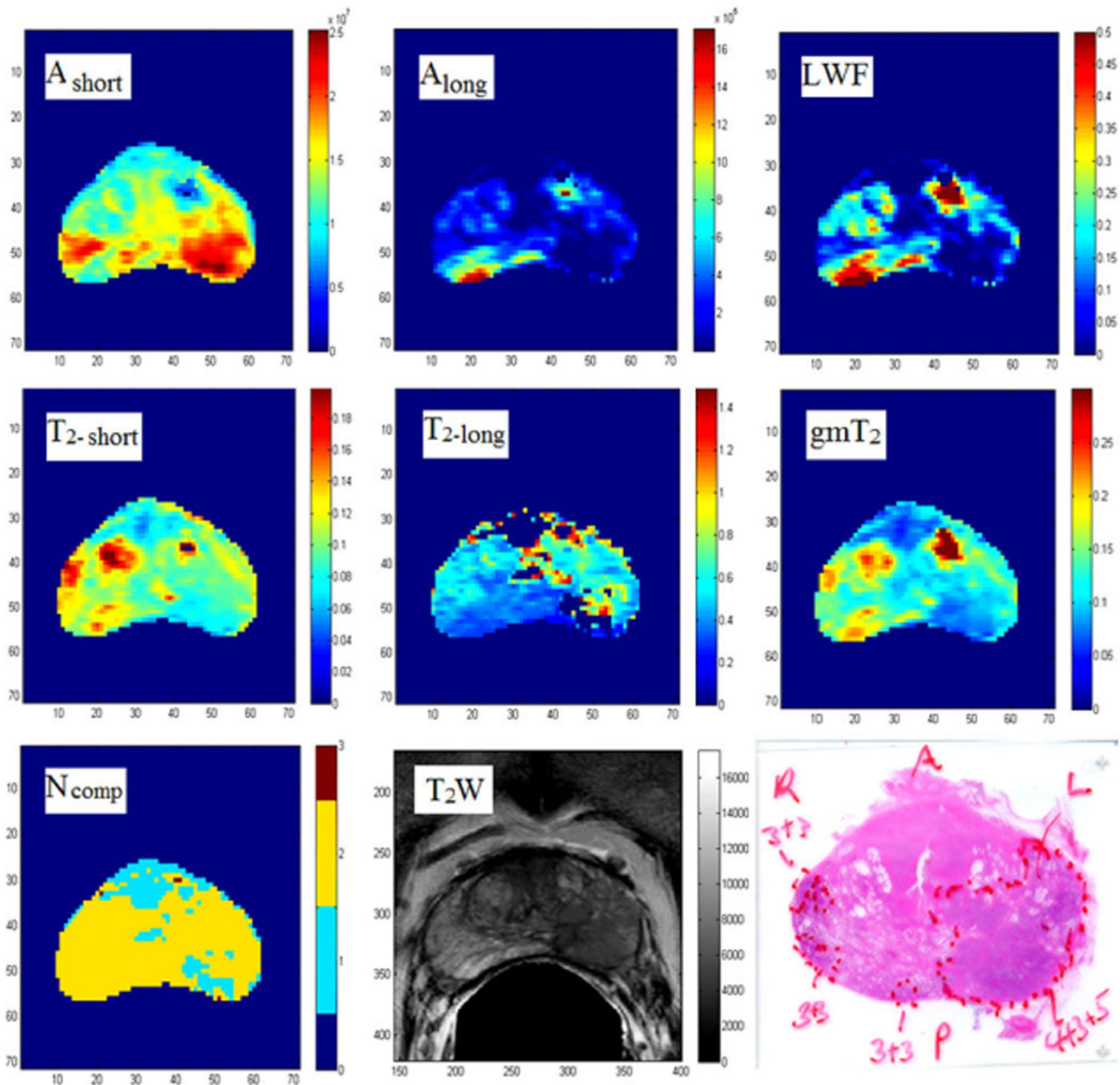Prostate tissue is composed of epithelium, stroma, and lumen. These glandular compartments have distinct

Fig. 7 A representative example of various maps of LWI. Representative maps of MR parameters, areas under the short (A_{short}) and long (A_{long}) T2 components, ratio of the area under the long component over the area under the entire distribution (LWF), the short T2 (T2-short) and long T2 (T2-long) components, and the geometric mean of the entire distribution (gmT2), Ncomp was obtained by counting the number of peaks in the distribution, axial T2-weighted image, and whole-mount histology of the same section (reproduced with permission from reference # 110 from John Wiley and Sons from Sabouri et al. 2017)

diffusivity and can shed light on various prostatic diseases [112]. The basis of HM-MRI is to assess changes in ADC and T2 values in response to variation in time to echo and b values. Further, employing a mathematical model prostatic tissue compositions can be measured using HM-MRI, non-invasively [113]. Wang et al. developed prostate HM-MRI method by taking into account the interdependence of ADC and T2 values, and measuring the ADC as a function of TE and the T2 as a function of b value [114]. The fractional volumes of stroma, epithelium, and lumen of prostate were obtained by Chatterjee et al. by fitting the HM-MRI data to a three compartment models [113]. Compared to normal prostatic tissue, PCa showed increased epithelium, a decrease in lumen and stroma [113] (Fig. 8). Motion-induced artefacts due to a long acquisition time are one of the challenges with HM-MRI.

Fig. 8 A 56-year-old man with Gleason score 4 + 3 cancer in right peripheral zone. The cancer lesion (arrows) shows reduced stroma (36.4%) and lumen (7.8%) volume and elevated epithelium volume (55.8%) compared to surrounding benign tissue. HM-MRI correctly predicts it be a clinically significant cancer on the predicted cancer map, and seen as hypointense region in the corresponding T2-weighted image (courtesy of Prof. A. Oto and Dr A. Chatterjee, University of Chicago)
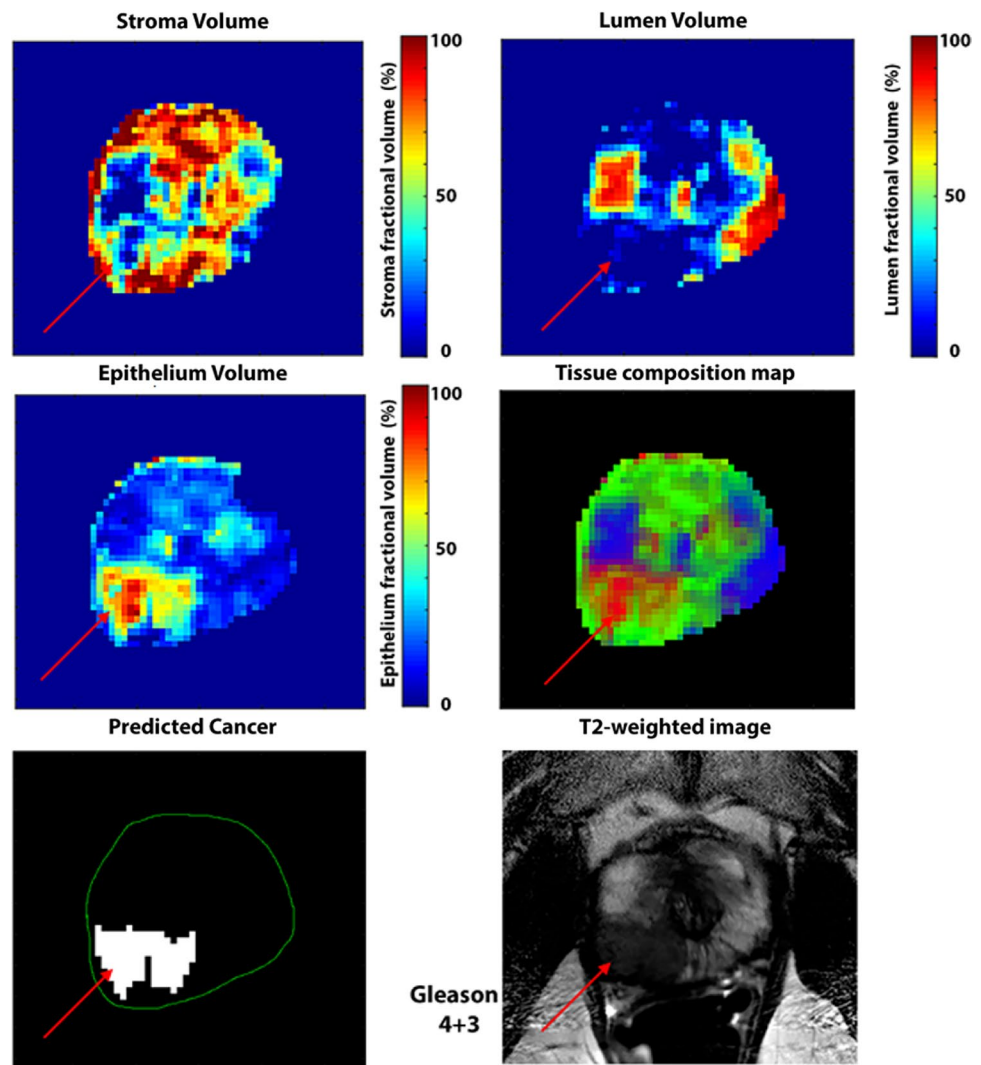
Chemical exchange saturation transfer (CEST) imaging

CEST is a molecular imaging method that maps the exchange between protons of the bulk water and protons in small metabolites and macromolecules [115, 116]. It enables us to image the low concentration compounds that often cannot be detected by conventional MRI or MRS. In CEST, exchangeable solute protons resonating at a different frequency than bulk water proton are selectively saturated using radiofrequency irradiation [115]. Acquisition of CEST involves radiofrequency saturation (e.g., using a continuous wave or short pulsed saturation) at different spectral positions followed by standard data acquisition using a single shot EPI. In CEST, water signal gets changed depending upon the target molecule with varying frequency offsets; thus, we generate a map of the normalized water signal intensity as a function of the frequency of the off-resonance saturation known as Z-spectrum.

The detection of exchangeable amide proton of peptides and proteins, also known as amide proton transfer (APT) imaging, is the most commonly studied signals in CEST imaging [117].

In a preliminary study, Jia et al. showed that APT ratio was significantly higher in PCa than benign regions ($5.8\% \pm 3.2\%$ vs $0.3\% \pm 3.2\%$, $p = 0.002$) [118]. Takayama et al. characterized 66 biopsy proven PCa by APT imaging and analyzed one slice per patient [119]. The mean APT signal obtained was highest for patients with GS 7 than the other GS categories (GS-6: 2.48 ± 0.59; GS-7: 5.17 ± 0.66, GS-8: 2.56 ± 0.85, and GS-9: 1.96 ± 0.75) [119]. DKI and APT were also used in assessing risk assessment of PCa and it was found that both the DKI and APT derived parameters are valuable in the diagnosis and segregation of PCa [120]. Often CEST suffers from B0 or B1 inhomogeneity and motion-related artifacts. Further large cohort studies are needed to prove the role of CEST imaging in detection and characterization of PCa.

MR Fingerprinting and other MR methods

Ma et al. were the first to propose MR fingerprinting (MRF), an innovative approach for obtaining quantitative measurements of several MR parameters in a single session [121]. It enables simultaneous measurement of quantitative maps of T1, T2, and proton density. Signal evolution or 'fingerprints' provide the unique characteristic of tissue. With the use of optimized repetition time, flip angle, and sampling patterns in a pseudo-random manner, a dictionary of signal evolution using Bloch simulation are generated [14]. These dictionary values are used to assign T1 and T2 values and other tissue properties.

MRF was previously acquired using the balanced steady-state free precession (bSSFP) sequence; however due to B0 inhomogeneity, it is now obtained using a fast imaging with steady-state precession (FISP). MRF has been utilized in various diseases including PCa [122–124]. Panda et al. evaluated MRF combined with ADC mapping to characterize TZ PCa lesions [123], (Fig. 9). TZ cancers had lower T1, T2, and ADC than non-cancers. While MRF

allows fast, simultaneous generation of quantitative maps of multiple physical properties such as T1 and T2, it will be interesting to study how this can be incorporated to standard mpMRI of prostate.

Beside these, a few other MR methods have recently demonstrated their potential in PCa. Briefly, the stimulated-echo-based mapping (STEM) approach for simultaneous T1, T2, and ADC mapping showed improved image quality in PCa detection [125, 126]. MR elastography revealed that PCa had a higher mean elasticity than benign disease [127, 128]. Another MR method, high spectral and spatial resolution (HiSS) MRI, has shown its potential in breast cancer and PCa [129, 130]. HiSS is a kind of spectroscopic imaging; however, it focuses on water and fat resonance, allowing proper elimination of fat resonance. It can also provide subvoxel tissue structure including vascularity of tissue of interest. Further, initial studies have shown feasibility of 7 T MR in the diagnosis of PCa [97, 131]. But, it suffers from challenges like substantial non-uniformities in B1 field and radiofrequency power deposition.
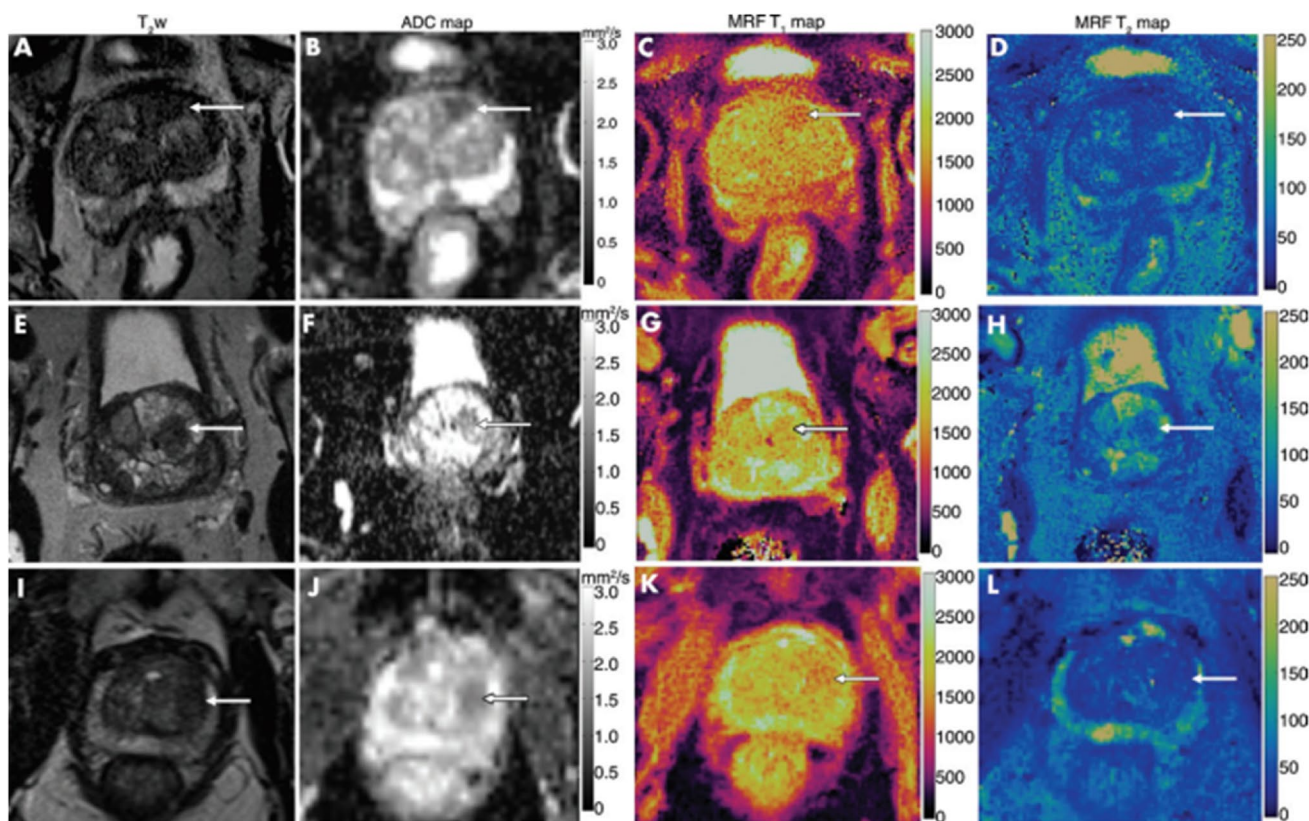

Fig. 9 A representative example of MR fingerprinting. T2W, ADC map, MR fingerprinting (MRF) T1 map, and MRF T2map for biopsy proven PCa **A–D**; prostatitis **E–H**, and a benign prostatic hyperplasia (BPH) nodule (**I–L**). **A–D** for PCa (arrow), mean T1, T2, and ADC were 1450 ms, 43 ms, and 0.51×10^{-3} mm^2/sec, respectively. **E–H**: for prostatitis (arrow), Mean T1, T2, and ADC were 1615 ms, 63 ms, and 0.83×10^{-3} mm^2/sec, respectively. **I–L**: for BPH nodule (arrow), mean T1, T2, and ADC were 1600 ms, 43 ms, and 0.87×10^{-3} mm^2/sec, respectively (reproduced with permission from reference # 123 from the Radiology Society of North America (RSNA) from Panda et al. 2019)

Quantitative MRI parameters and computational methods

Diffusion metric and diffusion–MR-based methods

DWI provides contrast based on the average water molecule displacement over a specific time interval in biological tissues. The most commonly used mono-exponential way to describe the attenuated diffusion weighted (DW) signal, known as the ADC, has been the cornerstone of prostate mpMRI. Previous studies have found an inverse relationship between ADC and Gleason grades [3]. Kumar et al. reported a mean ADC value of $1.68 \pm 0.31 \times 10^{-3}$ mm^2/s for the PZ compared with $1.07 \pm 0.25 \times 10^{-3}$ mm^2/s obtained for the central gland in healthy volunteers [19]. They also obtained a cutoff value of 1.17×10^{-3} mm^2/s to predict PCa, while Nagayama et al. reported a cutoff value of 1.35×10^{-3} mm^2/s with an accuracy of 93% [19, 132]. Further, in PZ PCa, DWI outperformed quantitative T2 and DCE- MRI [133]. As per a systematic review and meta-analysis, the pooled mean ADC of clinically significant PCa was 0.86×10^{-3} mm^2/s while the pooled mean ADC of insignificant PCa was 1.1×10^{-3} mm^2/s [134]. This shows that despite having advantage of oversimplified mean ADC, there is significant overlap in reported values partly due to variations in acquisition methods and use of varying *b* values.

In order to improve repeatability and applicability, several alternative ADC quantitative metrics have been used by various groups to diagnose PCa, e.g., the ADC ratio, which is the mean ADC of tumor to the mean ADC of normal tissue. ADC ratio was shown to have the best AUC value for differentiating low-grade from high-grade PCa [135]. Similarly, the ADC histogram has been used to assess the heterogeneity of PCa, and it was observed that the 10th percentile ADC is a better predictor in differentiating various Gleason grades [136]. Several other non-Gaussian DW-related quantitative parameters such as kurtosis, perfusion fraction, bi-exponential diffusion, and pseudo-diffusion are also under investigation for their clinical potentials in the improved diagnosis of PCa which has been discussed previously [47, 53].

Radiomic analyses of mpMRI in PCa and machine and deep learning methods

In addition to the development of novel MR sequences and techniques, recent improvements have been made in texture analysis, radiomics, and radiogenomics to find new biomarkers for PCa and to assess heterogeneity of the disease. Texture analysis provides quantitative imaging features, particularly using the second and higher-order texture descriptors like gray-level co-occurrence matrix (GLCM) and gray-level run length matrix (GLRLM) [137, 138]. A variety of methods, including first-order statistics and Haralick texture features, have been applied to a wide range of malignancies [139, 140]. Radiomics is a process that involves extracting quantitative features from radiographic images using computational algorithms, whereas radiogenomics aims to correlate imaging features to biological and genomic data [141–144]. The combination of these –omics approaches would differentiate between indolent and aggressive PCa, allowing for a more tailored approach to PCa management. These methods require a huge amount of data, and care should be taken while selecting stable features to ensure that results are reproducible. Stoyanova et al. performed a radiogenomics analysis to assess the relationship between radiomic features and RNA data obtained from microarray from 17 biopsies from 6 PCa patients [141]. A distinct phenotypic difference was found indicating the multifocality and heterogeneity of PCa.

Furthermore, in the era of big data and artificial intelligence (AI), such information could be used to develop computer-aided decision-making systems. Machine learning, a subfield of AI is reshaping the healthcare industry [145]. Machine learning applications to prostate mpMRI can be used to perform image segmentation, registration of TRUS/MR images for biopsy, image reconstruction, detection, and characterization of PCa.

In a multicenter study, the Prostate MR Image Segmentation (PROMISE12) challenge was set up for prostate segmentation on 100 patients [146]. Two automatic algorithms, Imorphics, and ScrAutoProstate were fast and outperformed the other algorithms [146]. Tian et al. utilized a convolutional neural network (CNN) model to segment prostate on T2W MR images [147]. As compared to manually labeled ground truth, the CNN model achieved a mean Dice similarity coefficient (DSC) of $85 \pm 3.8\%$ [147]. Another study developed a fully automated cascaded U-Net model for segmentation using T2W and DWI that resulted in a higher mean DSC ($92.7 \pm 4.2\%$) for the entire prostate gland and $79.3 \pm 10.4\%$ for the PZ [148]. Dai et al. developed a mask region-based CNN model to segment the prostate and segment the prostate lesions [149]. The model automatically segmented the entire prostate and identified highly suspicious prostate lesions. The promising results of the PROSTATEx challenge prompted machine learning enthusiasts to plan further studies to automatically characterize PCa lesions [150, 151]. Wang et al. proposed an end-to-end trainable deep neural network for automatic detection of PCa and multimodal registration, and characterization of PCa [151]. A recent systematic review analyzed the ability of fully automated deep learning and semi-automated
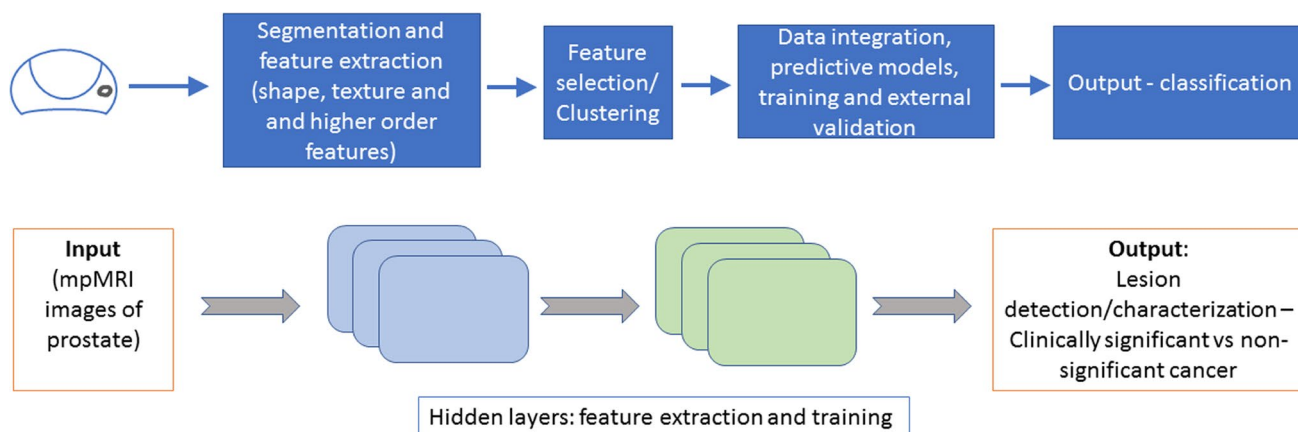
Fig. 10 Artificial intelligence pipelines. The top panel shows radiomics and traditional machine learning approach. The bottom panel shows the deep learning approaches such as a typical convolution neural network (CNN) where feature extraction, pooling, and finally connected layers can be used for classification and simultaneously to predict the outcome

traditional machine learning for the detection of clinically significant PCa [152]. A comparable performance was observed of the two (fully automated and semi-automated) AI methods. However, it identified several methodological issues and biases (e.g., inappropriate ground truth, lack of multi-reader image segmentation, and single center datasets without external test cohorts) that must be handled in future studies to make sure created models are generalizable [152].

The accurate curation of medical data is a key challenge in establishing fully automated AI-based clinical solutions. Another issue is the scarcity of large amounts of labeled data, which limits the full potential of deep learning methods. Moreover, suboptimal quality of data can make it difficult to design fully automated AI-based clinical solutions.

Summary and future directions

The developments of novel mpMRI methods promise accuracy and unique knowledge of microstructural changes in malignant prostate tissue. An mpMRI is highly powerful method but for its wider applicability and translating it as a screening method of PCa, researchers need to come up with faster and cost-effective MR methods to reduce the acquisition time, along with optimized protocols [153]. Further, the rule-in ability of mpMRI in previous negative biopsy needs further evaluation due to a large variability in positive predictive value. Also, there is a need to develop a multidisciplinary approach that includes radiologists, researchers, physicists, and urologists who understand the unmet clinical needs and technological advances in order to redefine the approaches that can further improve upon the ability of mpMRI in diagnosis and characterization of PCa. Uniform MR protocol with an optimal image quality and appropriate training of radiologists are key

factors in detecting clinically significant PCa. Faster sampling methods, non-Cartesian acquisition such as radial k-space sampling have improved the accuracy and to a certain extent mitigated motion related issues in prostate mpMRI. Various newer MR methods such as MRF, HM-MRI, RSI, VERDICT method, and LWI have provided an insight to prostatic microstructures. However, these methods should be used with caution because they are based on specific assumptions and are not always straightforward. HP ^{13}C-MRI and APT-MRI have also shown promising unique metabolic information in PCa. Aside from mpMRI advancements, Gallium-68-labeled prostate-specific membrane antigen (^{68}Ga-PSMA, e.g., US-FDA approved ligand ^{68}Ga-PSMA-11), a positron emission tomography (PET) tracer, has demonstrated potential in initial staging and biochemical recurrence for localized PCa [154].

Other than improvement in MR sequences, there has been tremendous progress made in image analysis methods. Radiomics and radiogenomics analyses, and advances in AI-based approaches particularly machine and deep learning methods (Fig. 10) are increasingly being used for image reconstruction, segmentation, and characterization of PCa lesions. These novel methods require prospective validation with high-quality data and reproducible outcomes before being incorporated in prostate mpMRI and clinical practice.

Author contributions DD made the literature survey. DD and NRJ drafted the manuscript and reviewed.

Declarations

Conflicts of interest None.

References

1. Siegel RL, Miller KD, Fuchs HE, Jemal A (2022) Cancer statistics, 2022. CA Cancer J Clin. https://doi.org/10.3322/caac.21708

2. Etzioni R, Penson DF, Legler JM, di Tommaso D, Boer R, Gann PH, Feuer EJ (2002) Overdiagnosis due to prostate-specific antigen screening: lessons from U.S. prostate cancer incidence trends. J Natl Cancer Inst 94(13):981–990

3. Dwivedi DK, Kumar R, Bora GS, Thulkar S, Sharma S, Gupta SD, Jagannathan NR (2016) Stratification of the aggressiveness of prostate cancer using pre-biopsy multiparametric MRI (mpMRI). NMR Biomed 29(3):232–238

4. Kumar R, Nayyar R, Kumar V, Gupta NP, Hemal AK, Jagannathan NR, Dattagupta S, Thulkar S (2008) Potential of magnetic resonance spectroscopic imaging in predicting absence of prostate cancer in men with serum prostate-specific antigen between 4 and 10 ng/ml: a follow-up study. Urology 72(4):859–863

5. Vargas HA, Akin O, Franiel T, Mazaheri Y, Zheng J, Moskowitz C, Udo K, Eastham J, Hricak H (2011) Diffusion-weighted endorectal MR imaging at 3 T for prostate cancer: tumor detection and assessment of aggressiveness. Radiology 259(3):775–784

6. Costa DN, Xi Y, Aziz M, Passoni N, Shakir N, Goldberg K, Francis F, Roehrborn CG, Leon AD, Pedrosa I (2019) Prospective inclusion of apparent diffusion coefficients in multiparametric prostate MRI structured reports: discrimination of clinically insignificant and significant cancers. AJR Am J Roentgenol 212(1):109–116

7. Turkbey B, Rosenkrantz AB, Haider MA, Padhani AR, Villeirs G, Macura KJ, Tempany CM, Choyke PL, Cornud F, Margolis DJ, Thoeny HC, Verma S, Barentsz J, Weinreb JC (2019) Prostate imaging reporting and data system version 2.1:2019 update of Prostate imaging reporting and data system version 2. Eur Urol 76(3):340–351

8. Iima M, Le Bihan D (2016) Clinical intravoxel incoherent motion and diffusion mr imaging: past, present, and future. Radiology 278(1):13–32

9. Jagannathan NR, Kumar V, Kumar R, Thulkar S (2008) Role of magnetic resonance methods in the evaluation of prostate cancer: an Indian perspective. MAGMA 21(6):393–407

10. Schieda N, Lim CS, Zabihollahy F, Abreu-Gomez J, Krishna S, Woo S, Melkus G, Ukwatta E, Turkbey B (2021) Quantitative prostate MRI. J Magn Reson Imaging 53(6):1632–1645

11. Stabile A, Giganti F, Kasivisvanathan V, Giannarini G, Moore CM, Padhani AR, Panebianco V, Rosenkrantz AB, Salomon G, Turkbey B, Villeirs G, Barentsz JO (2020) Factors influencing variability in the performance of multiparametric magnetic resonance imaging in detecting clinically significant prostate cancer: a systematic literature review. Eur Urol Oncol 3(2):145–167

12. Drost FH, Osses DF, Nieboer D, Steyerberg EW, Bangma CH, Roobol MJ, Schoots IG (2019) Prostate MRI, with or without MRI-targeted biopsy, and systematic biopsy for detecting prostate cancer. Cochrane Database Syst Rev 4:CD012663.

13. Niaf E, Lartizien C, Bratan F, Roche L, Rabilloud M, Mege-Lechevallier F, Rouviere O (2014) Prostate focal peripheral zone lesions: characterization at multiparametric MR imaging–influence of a computer-aided diagnosis system. Radiology 271(3):761–769

14. Jiang Y, Ma D, Seiberlich N, Gulani V, Griswold MA (2015) MR fingerprinting using fast imaging with steady state precession (FISP) with spiral readout. Magn Reson Med 74(6):1621–1631

15. Ilic D, Neuberger MM, Djulbegovic M, Dahm P (2013) Screening for prostate cancer. Cochrane Database Syst Rev. https://doi.org/10.1002/14651858.CD004720.pub3(1):CD004720

16. Mottet N, van den Bergh RCN, Briers E, Van den Broeck T, Cumberbatch MG, De Santis M, Fanti S, Fossati N, Gandaglia G, Gillessen S, Grivas N, Grummet J, Henry AM, van der Kwast TH, Lam TB, Lardas M, Liew M, Mason MD, Moris L, Oprea-Lager DE, van der Poel HG, Rouviere O, Schoots IG, Tilki D, Wiegel T, Willemse PM, Cornford P (2021) EAU-EANM-ESTRO-ESUR-SIOG guidelines on prostate cancer-2020 Update. Part 1: screening, diagnosis, and local treatment with curative intent. Eur Urol 79(2):243–262

17. Norris JM, Carmona Echeverria LM, Bott SRJ, Brown LC, Burns-Cox N, Dudderidge T, El-Shater Bosaily A, Frangou E, Freeman A, Ghei M, Henderson A, Hindley RG, Kaplan RS, Kirkham A, Oldroyd R, Parker C, Persad R, Punwani S, Rosario DJ, Shergill IS, Stavrinides V, Winkler M, Whitaker HC, Ahmed HU, Emberton M (2020) What type of prostate cancer is systematically overlooked by multiparametric magnetic resonance imaging? An analysis from the PROMIS Cohort. Eur Urol 78(2):163–170

18. Rouviere O, Puech P, Renard-Penna R, Claudon M, Roy C, Mege-Lechevallier F, Decaussin-Petrucci M, Dubreuil-Chambardel M, Magaud L, Remontet L, Ruffion A, Colombel M, Crouzet S, Schott AM, Lemaitre L, Rabilloud M, Grenier N, Investigators M-F (2019) Use of prostate systematic and targeted biopsy on the basis of multiparametric MRI in biopsy-naive patients (MRI-FIRST): a prospective, multicentre, paired diagnostic study. Lancet Oncol 20(1):100–109

19. Kumar V, Jagannathan NR, Kumar R, Thulkar S, Gupta SD, Dwivedi SN, Hemal AK, Gupta NP (2007) Apparent diffusion coefficient of the prostate in men prior to biopsy: determination of a cut-off value to predict malignancy of the peripheral zone. NMR Biomed 20(5):505–511

20. Kumar V, Jagannathan NR, Kumar R, Thulkar S, Gupta SD, Hemal AK, Gupta NP (2007) Transrectal ultrasound-guided biopsy of prostate voxels identified as suspicious of malignancy on three-dimensional (1)H MR spectroscopic imaging in patients with abnormal digital rectal examination or raised prostate specific antigen level of 4–10 ng/ml. NMR Biomed 20(1):11–20

21. Ahmed HU, El-Shater Bosaily A, Brown LC, Gabe R, Kaplan R, Parmar MK, Collaco-Moraes Y, Ward K, Hindley RG, Freeman A, Kirkham AP, Oldroyd R, Parker C, Emberton M, group Ps (2017) Diagnostic accuracy of multi-parametric MRI and TRUS biopsy in prostate cancer (PROMIS): a paired validating confirmatory study. Lancet 389(10071):815–822

22. Kuhl CK, Bruhn R, Kramer N, Nebelung S, Heidenreich A, Schrading S (2017) Abbreviated biparametric prostate MR imaging in men with elevated prostate-specific antigen. Radiology 285(2):493–505

23. Thestrup KC, Logager V, Baslev I, Moller JM, Hansen RH, Thomsen HS (2016) Biparametric versus multiparametric MRI in the diagnosis of prostate cancer. Acta Radiol Open 5(8):2058460116663046

24. Eldred-Evans D, Tam H, Sokhi H, Padhani AR, Winkler M, Ahmed HU (2020) Rethinking prostate cancer screening: could MRI be an alternative screening test? Nat Rev Urol 17(9):526–539

25. Eklund M, Jaderling F, Discacciati A, Bergman M, Annerstedt M, Aly M, Glaessgen A, Carlsson S, Gronberg H, Nordstrom T, consortium S (2021) MRI-Targeted or standard biopsy in prostate cancer screening. N Engl J Med 385(10):908–920

26. Barentsz JO, Choyke PL, Cornud F, Haider MA, Macura KJ, Margolis D, Shtern F, Padhani AR, Tempany CM, Thoeny HC, Verma S, Weinreb JC (2016) Reply to Erik Rud and Eduard Baco's Letter to the Editor re: Re: Jeffrey C. Weinreb, Jelle O. Barentsz, Peter L. Choyke, et al. PI-RADS Prostate Imaging - Reporting and Data System: 2015, Version 2. Eur Urol 2016;69:16–40. Eur Urol 70 (5):e137–e138.

27. Woo S, Suh CH, Kim SY, Cho JY, Kim SH (2017) Diagnostic performance of prostate imaging reporting and data system version 2 for detection of prostate cancer: a systematic review and diagnostic meta-analysis. Eur Urol 72(2):177–188

28. Giganti F, Allen C, Emberton M, Moore CM, Kasivisvanathan V, group Ps (2020) Prostate imaging quality (PI-QUAL): a new quality control scoring system for multiparametric magnetic resonance imaging of the prostate from the PRECISION trial. Eur Urol Oncol 3(5):615–619

29. Reischauer C, Cancelli T, Malekzadeh S, Froehlich JM, Thoeny HC (2021) How to improve image quality of DWI of the prostate-enema or catheter preparation? Eur Radiol. https://doi.org/10.1007/s00330-021-07842-9

30. Kasivisvanathan V, Rannikko AS, Borghi M, Panebianco V, Mynderse LA, Vaarala MH, Briganti A, Budaus L, Hellawell G, Hindley RG, Roobol MJ, Eggener S, Ghei M, Villers A, Bladou F, Villeirs GM, Virdi J, Boxler S, Robert G, Singh PB, Venderink W, Hadaschik BA, Ruffion A, Hu JC, Margolis D, Crouzet S, Klotz L, Taneja SS, Pinto P, Gill I, Allen C, Giganti F, Freeman A, Morris S, Punwani S, Williams NR, Brew-Graves C, Deeks J, Takwoingi Y, Emberton M, Moore CM, PSG Collaborators (2018) MRI-targeted or standard biopsy for prostate-cancer diagnosis. N Engl J Med 378(19):1767–1777

31. Klotz L, Chin J, Black PC, Finelli A, Anidjar M, Bladou F, Mercado A, Levental M, Ghai S, Chang SD, Milot L, Patel C, Kassam Z, Moore C, Kasivisvanathan V, Loblaw A, Kebabdjian M, Earle CC, Pond GR, Haider MA (2021) Comparison of multiparametric magnetic resonance imaging-targeted biopsy with systematic transrectal ultrasonography biopsy for biopsy-naive men at risk for prostate cancer: a phase 3 randomized clinical trial. JAMA Oncol 7(4):534–542

32. Dwivedi DK, Kumar R, Dwivedi AK, Bora GS, Thulkar S, Sharma S, Gupta SD, Jagannathan NR (2018) Prebiopsy multiparametric MRI-based risk score for predicting prostate cancer in biopsy-naive men with prostate-specific antigen between 4–10 ng/mL. J Magn Reson Imaging 47(5):1227–1236

33. Dirix P, Van Bruwaene S, Vandeursen H, Deckers F (2019) Magnetic resonance imaging sequences for prostate cancer triage: two is a couple, three is a crowd? Transl Androl Urol 8(Suppl 5):S476–S479

34. Schoots IG, Petrides N, Giganti F, Bokhorst LP, Rannikko A, Klotz L, Villers A, Hugosson J, Moore CM (2015) Magnetic resonance imaging in active surveillance of prostate cancer: a systematic review. Eur Urol 67(4):627–636

35. Moldovan PC, Van den Broeck T, Sylvester R, Marconi L, Bellmunt J, van den Bergh RCN, Bolla M, Briers E, Cumberbatch MG, Fossati N, Gross T, Henry AM, Joniau S, van der Kwast TH, Matveev VB, van der Poel HG, De Santis M, Schoots IG, Wiegel T, Yuan CY, Cornford P, Mottet N, Lam TB, Rouviere O (2017) What Is the negative predictive value of multiparametric magnetic resonance imaging in excluding prostate cancer at biopsy? a systematic review and meta-analysis from the european association of urology prostate cancer guidelines panel. Eur Urol 72(2):250–266

36. Arsov C, Rabenalt R, Blondin D, Quentin M, Hiester A, Godehardt E, Gabbert HE, Becker N, Antoch G, Albers P, Schimmoller L (2015) Prospective randomized trial comparing magnetic resonance imaging (MRI)-guided in-bore biopsy to MRI-ultrasound fusion and transrectal ultrasound-guided prostate biopsy in patients with prior negative biopsies. Eur Urol 68(4):713–720

37. Wibmer AG, Chaim J, Lakhman Y, Lefkowitz RA, Nincevic J, Nikolovski I, Sala E, Gonen M, Carlsson SV, Fine SW, Zelefsky MJ, Scardino P, Hricak H, Vargas HA (2021) Oncologic outcomes after localized prostate cancer treatment: associations with pretreatment prostate magnetic resonance imaging findings. J Urol 205(4):1055–1062

38. Boesen L, Norgaard N, Logager V, Balslev I, Bisbjerg R, Thestrup KC, Winther MD, Jakobsen H, Thomsen HS (2018) Assessment of the diagnostic accuracy of biparametric magnetic resonance imaging for prostate cancer in biopsy-naive men: the biparametric MRI for detection of prostate cancer (BIDOC) study. JAMA Netw Open 1(2):e180219

39. Le Bihan D, Breton E, Lallemand D, Grenier P, Cabanis E, Laval-Jeantet M (1986) MR imaging of intravoxel incoherent motions: application to diffusion and perfusion in neurologic disorders. Radiology 161(2):401–407

40. Chandarana H, Kang SK, Wong S, Rusinek H, Zhang JL, Arizono S, Huang WC, Melamed J, Babb JS, Suan EF, Lee VS, Sigmund EE (2012) Diffusion-weighted intravoxel incoherent motion imaging of renal tumors with histopathologic correlation. Invest Radiol 47(12):688–696

41. Riches SF, Hawtin K, Charles-Edwards EM, de Souza NM (2009) Diffusion-weighted imaging of the prostate and rectal wall: comparison of biexponential and monoexponential modelled diffusion and associated perfusion coefficients. NMR Biomed 22(3):318–325

42. Sigmund EE, Cho GY, Kim S, Finn M, Moccaldi M, Jensen JH, Sodickson DK, Goldberg JD, Formenti S, Moy L (2011) Intravoxel incoherent motion imaging of tumor microenvironment in locally advanced breast cancer. Magn Reson Med 65(5):1437–1447

43. Shinmoto H, Tamura C, Soga S, Shiomi E, Yoshihara N, Kaji T, Mulkern RV (2012) An intravoxel incoherent motion diffusion-weighted imaging study of prostate cancer. AJR Am J Roentgenol 199(4):W496-500

44. Pang Y, Turkbey B, Bernardo M, Kruecker J, Kadoury S, Merino MJ, Wood BJ, Pinto PA, Choyke PL (2013) Intravoxel incoherent motion MR imaging for prostate cancer: an evaluation of perfusion fraction and diffusion coefficient derived from different b-value combinations. Magn Reson Med 69(2):553–562

45. Chatterjee A, Watson G, Myint E, Sved P, McEntee M, Bourne R (2015) Changes in epithelium, stroma, and lumen space correlate more strongly with gleason pattern and are stronger predictors of prostate ADC changes than cellularity metrics. Radiology 277(3):751–762

46. Jensen JH, Helpern JA, Ramani A, Lu H, Kaczynski K (2005) Diffusional kurtosis imaging: the quantification of non-gaussian water diffusion by means of magnetic resonance imaging. Magn Reson Med 53(6):1432–1440

47. Brancato V, Cavaliere C, Salvatore M, Monti S (2019) Non-Gaussian models of diffusion weighted imaging for detection and characterization of prostate cancer: a systematic review and meta-analysis. Sci Rep 9(1):16837

48. Roethke MC, Kuder TA, Kuru TH, Fenchel M, Hadaschik BA, Laun FB, Schlemmer HP, Stieltjes B (2015) Evaluation of diffusion kurtosis imaging versus standard diffusion imaging for detection and grading of peripheral zone prostate cancer. Invest Radiol 50(8):483–489

49. Wu CJ, Zhang YD, Bao ML, Li H, Wang XN, Liu XS, Shi HB (2017) Diffusion kurtosis imaging helps to predict upgrading in biopsy-proven prostate cancer with a gleason score of 6. AJR Am J Roentgenol 209(5):1081–1087

50. Si Y, Liu RB (2018) Diagnostic performance of monoexponential DWI versus diffusion kurtosis imaging in prostate cancer:

a systematic review and meta-analysis. AJR Am J Roentgenol 211(2):358–368

51. Shan Y, Chen X, Liu K, Zeng M, Zhou J (2019) Prostate cancer aggressive prediction: preponderant diagnostic performances of intravoxel incoherent motion (IVIM) imaging and diffusion kurtosis imaging (DKI) beyond ADC at 3.0 T scanner with gleason score at final pathology. Abdom Radiol (NY) 44(10):3441–3452

52. Feng Z, Min X, Margolis DJ, Duan C, Chen Y, Sah VK, Chaudhary N, Li B, Ke Z, Zhang P, Wang L (2017) Evaluation of different mathematical models and different b-value ranges of diffusion-weighted imaging in peripheral zone prostate cancer detection using b-value up to 4500 s/mm2. PLoS ONE 12(2):e0172127

53. McGarry SD, Brehler M, Bukowy JD, Lowman AK, Bobholz SA, Duenweg SR, Banerjee A, Hurrell SL, Malyarenko D, Chenevert TL, Cao Y, Li Y, You D, Fedorov A, Bell LC, Quarles CC, Prah MA, Schmainda KM, Taouli B, LoCastro E, Mazaheri Y, Shukla-Dave A, Yankeelov TE, Hormuth DA 2nd, Madhuranthakam AJ, Hulsey K, Li K, Huang W, Huang W, Muzi M, Jacobs MA, Solaiyappan M, Hectors S, Antic T, Paner GP, Palangmonthip W, Jacobsohn K, Hohenwalter M, Duvnjak P, Griffin M, See W, Nevalainen MT, Iczkowski KA, LaViolette PS (2021) Multi-site concordance of diffusion-weighted imaging quantification for assessing prostate cancer aggressiveness. J Magn Reson Imaging. https://doi.org/10.1002/jmri.27983

54. Lu Y, Jansen JF, Mazaheri Y, Stambuk HE, Koutcher JA, Shukla-Dave A (2012) Extension of the intravoxel incoherent motion model to non-gaussian diffusion in head and neck cancer. J Magn Reson Imaging 36(5):1088–1096

55. Malagi AV, Netaji A, Kumar V, Baidya Kayal E, Khare K, Das CJ, Calamante F, Mehndiratta A (2021) IVIM-DKI for differentiation between prostate cancer and benign prostatic hyperplasia: comparison of 1.5 T vs. 3 T MRI. MAGMA. https://doi.org/10.1007/s10334-021-00932-1

56. Hectors SJ, Semaan S, Song C, Lewis S, Haines GK, Tewari A, Rastinehad AR, Taouli B (2018) Advanced diffusion-weighted imaging modeling for prostate cancer characterization: correlation with quantitative histopathologic tumor tissue composition-a hypothesis-generating study. Radiology 286(3):918–928

57. Nilsson M, Eklund G, Szczepankiewicz F, Skorpil M, Bryskhe K, Westin CF, Lindh C, Blomqvist L, Jaderling F (2021) Mapping prostatic microscopic anisotropy using linear and spherical b-tensor encoding: A preliminary study. Magn Reson Med 86(4):2025–2033

58. Westin CF, Szczepankiewicz F, Pasternak O, Ozarslan E, Topgaard D, Knutsson H, Nilsson M (2014) Measurement tensors in diffusion MRI: generalizing the concept of diffusion encoding. Med Image Comput Comput Assist Interv 17(Pt 3):209–216

59. Rakow-Penner RA, White NS, Parsons JK, Choi HW, Liss MA, Kuperman JM, Schenker-Ahmed N, Bartsch H, Mattrey RF, Bradley WG, Shabaik A, Huang J, Margolis DJ, Raman SS, Marks L, Kane CJ, Reiter RE, Karow DS, Dale AM (2015) Novel technique for characterizing prostate cancer utilizing MRI restriction spectrum imaging: proof of principle and initial clinical experience with extraprostatic extension. Prostate Cancer Prostatic Dis 18(1):81–85

60. White NS, Leergaard TB, D'Arceuil H, Bjaalie JG, Dale AM (2013) Probing tissue microstructure with restriction spectrum imaging: Histological and theoretical validation. Hum Brain Mapp 34(2):327–346

61. White NS, McDonald C, Farid N, Kuperman J, Karow D, Schenker-Ahmed NM, Bartsch H, Rakow-Penner R, Holland D, Shabaik A, Bjornerud A, Hope T, Hattangadi-Gluth J, Liss M, Parsons JK, Chen CC, Raman S, Margolis D, Reiter RE, Marks L, Kesari S, Mundt AJ, Kane CJ, Carter BS, Bradley WG, Dale AM (2014) Diffusion-weighted imaging in cancer: physical foundations and applications of restriction spectrum imaging. Cancer Res 74(17):4638–4652

62. Brunsing RL, Schenker-Ahmed NM, White NS, Parsons JK, Kane C, Kuperman J, Bartsch H, Kader AK, Rakow-Penner R, Seibert TM, Margolis D, Raman SS, McDonald CR, Farid N, Kesari S, Hansel D, Shabaik A, Dale AM, Karow DS (2017) Restriction spectrum imaging: An evolving imaging biomarker in prostate MRI. J Magn Reson Imaging 45(2):323–336

63. McCammack KC, Schenker-Ahmed NM, White NS, Best SR, Marks RM, Heimbigner J, Kane CJ, Parsons JK, Kuperman JM, Bartsch H, Desikan RS, Rakow-Penner RA, Liss MA, Margolis DJ, Raman SS, Shabaik A, Dale AM, Karow DS (2016) Restriction spectrum imaging improves MRI-based prostate cancer detection. Abdom Radiol (NY) 41(5):946–953

64. Felker ER, Raman SS, Shakeri S, Mirak SA, Bajgiran AM, Kwan L, Khoshnoodi P, ElKhoury FF, Margolis DJA, Karow D, Lu DSK, White N, Marks LS (2019) Utility of restriction spectrum imaging among men undergoing first-time biopsy for suspected prostate cancer. AJR Am J Roentgenol 213(2):365–370

65. Besasie BD, Sunnapwar AG, Gao F, Troyer D, Clarke GD, White H, Fox PT, Dale A, Wheeler A, Liss MA (2021) Restriction spectrum imaging-magnetic resonance imaging to improve prostate cancer imaging in men on active surveillance. J Urol 206(1):44–51

66. Panagiotaki E, Walker-Samuel S, Siow B, Johnson SP, Rajkumar V, Pedley RB, Lythgoe MF, Alexander DC (2014) Noninvasive quantification of solid tumor microstructure using VERDICT MRI. Cancer Res 74(7):1902–1912

67. Panagiotaki E, Chan RW, Dikaios N, Ahmed HU, O'Callaghan J, Freeman A, Atkinson D, Punwani S, Hawkes DJ, Alexander DC (2015) Microstructural characterization of normal and malignant human prostate tissue with vascular, extracellular, and restricted diffusion for cytometry in tumours magnetic resonance imaging. Invest Radiol 50(4):218–227

68. Bailey C, Bourne RM, Siow B, Johnston EW, Brizmohun Appayya M, Pye H, Heavey S, Mertzanidou T, Whitaker H, Freeman A, Patel D, Shaw GL, Sridhar A, Hawkes DJ, Punwani S, Alexander DC, Panagiotaki E (2019) VERDICT MRI validation in fresh and fixed prostate specimens using patient-specific moulds for histological and MR alignment. NMR Biomed 32(5):e4073

69. Johnston EW, Bonet-Carne E, Ferizi U, Yvernault B, Pye H, Patel D, Clemente J, Piga W, Heavey S, Sidhu HS, Giganti F, O'Callaghan J, Brizmohun Appayya M, Grey A, Saborowska A, Ourselin S, Hawkes D, Moore CM, Emberton M, Ahmed HU, Whitaker H, Rodriguez-Justo M, Freeman A, Atkinson D, Alexander D, Panagiotaki E, Punwani S (2019) VERDICT MRI for prostate cancer: intracellular volume fraction versus apparent diffusion coefficient. Radiology 291(2):391–397

70. Rosenkrantz AB, Chandarana H, Pfeuffer J, Triolo MJ, Shaikh MB, Mossa DJ, Geppert C (2015) Zoomed echo-planar imaging using parallel transmission: impact on image quality of diffusion-weighted imaging of the prostate at 3T. Abdom Imaging 40(1):120–126

71. Brendle C, Martirosian P, Schwenzer NF, Kaufmann S, Kruck S, Kramer U, Notohamiprodjo M, Nikolaou K, Schraml C (2016) Diffusion-weighted imaging in the assessment of prostate cancer: Comparison of zoomed imaging and conventional technique. Eur J Radiol 85(5):893–900

72. Eustace S, Tello R, DeCarvalho V, Carey J, Melhem E, Yucel EK (1998) Whole body turbo STIR MRI in unknown primary tumor detection. J Magn Reson Imaging 8(3):751–753

73. Padhani AR, Lecouvet FE, Tunariu N, Koh DM, De Keyzer F, Collins DJ, Sala E, Schlemmer HP, Petralia G, Vargas HA, Fanti S, Tombal HB, de Bono J (2017) METastasis reporting and data system for prostate cancer: practical guidelines for acquisition,

interpretation, and reporting of whole-body magnetic resonance imaging-based evaluations of multiorgan involvement in advanced prostate cancer. Eur Urol 71(1):81–92

74. Takahara T, Imai Y, Yamashita T, Yasuda S, Nasu S, Van Cauteren M (2004) Diffusion weighted whole body imaging with background body signal suppression (DWIBS): technical improvement using free breathing, STIR and high resolution 3D display. Radiat Med 22(4):275–282

75. Larbi A, Omoumi P, Pasoglou V, Michoux N, Triqueneaux P, Tombal B, Cyteval C, Lecouvet FE (2019) Whole-body MRI to assess bone involvement in prostate cancer and multiple myeloma: comparison of the diagnostic accuracies of the T1, short tau inversion recovery (STIR), and high b-values diffusion-weighted imaging (DWI) sequences. Eur Radiol 29(8):4503–4513

76. Kumasaka S, Motegi S, Kumasaka Y, Nishikata T, Otomo M, Tsushima Y (2021) Whole-body magnetic resonance imaging (WB-MRI) with diffusion-weighted whole-body imaging with background body signal suppression (DWIBS) in prostate cancer: Prevalence and clinical significance of incidental findings. Br J Radiol. https://doi.org/10.1259/bjr.20210459:20210459

77. Verma S, Turkbey B, Muradyan N, Rajesh A, Cornud F, Haider MA, Choyke PL, Harisinghani M (2012) Overview of dynamic contrast-enhanced MRI in prostate cancer diagnosis and management. AJR Am J Roentgenol 198(6):1277–1288

78. Tofts PS, Kermode AG (1991) Measurement of the blood-brain barrier permeability and leakage space using dynamic MR imaging. 1. Fundamental concepts. Magn Reson Med 17(2):357–367

79. Tofts PS, Brix G, Buckley DL, Evelhoch JL, Henderson E, Knopp MV, Larsson HB, Lee TY, Mayr NA, Parker GJ, Port RE, Taylor J, Weisskoff RM (1999) Estimating kinetic parameters from dynamic contrast-enhanced T(1)-weighted MRI of a diffusable tracer: standardized quantities and symbols. J Magn Reson Imaging 10(3):223–232

80. Palumbo P, Manetta R, Izzo A, Bruno F, Arrigoni F, De Filippo M, Splendiani A, Di Cesare E, Masciocchi C, Barile A (2020) Biparametric (bp) and multiparametric (mp) magnetic resonance imaging (MRI) approach to prostate cancer disease: a narrative review of current debate on dynamic contrast enhancement. Gland Surg 9(6):2235–2247

81. Rosenkrantz AB, Geppert C, Grimm R, Block TK, Glielmi C, Feng L, Otazo R, Ream JM, Romolo MM, Taneja SS, Sodickson DK, Chandarana H (2015) Dynamic contrast-enhanced MRI of the prostate with high spatiotemporal resolution using compressed sensing, parallel imaging, and continuous golden-angle radial sampling: preliminary experience. J Magn Reson Imaging 41(5):1365–1373

82. Chatterjee A, He D, Fan X, Wang S, Szasz T, Yousuf A, Pineda F, Antic T, Mathew M, Karczmar GS, Oto A (2018) Performance of ultrafast DCE-MRI for diagnosis of prostate cancer. Acad Radiol 25(3):349–358

83. Madhuranthakam AJ, Yuan Q, Pedrosa I (2017) Quantitative methods in abdominal MRI: perfusion imaging. Top Magn Reson Imaging 26(6):251–258

84. Haller S, Zaharchuk G, Thomas DL, Lovblad KO, Barkhof F, Golay X (2016) Arterial spin labeling perfusion of the brain: emerging clinical applications. Radiology 281(2):337–356

85. Li X, Metzger GJ (2013) Feasibility of measuring prostate perfusion with arterial spin labeling. NMR Biomed 26(1):51–57

86. Cai W, Li F, Wang J, Du H, Wang X, Zhang J, Fang J, Jiang X (2014) A comparison of arterial spin labeling perfusion MRI and DCE-MRI in human prostate cancer. NMR Biomed 27(7):817–825

87. Boschheidgen M, Schimmoller L, Kasprowski L, Abrar D, Arsov C, Albers P, Antoch G, Wittsack HJ, Ullrich T (2021) Arterial spin labelling as a gadolinium-free alternative in the detection of prostate cancer. Magn Reson Imaging 80:33–38

88. Ferre JC, Bannier E, Raoult H, Mineur G, Carsin-Nicol B, Gauvrit JY (2013) Arterial spin labeling (ASL) perfusion: techniques and clinical use. Diagn Interv Imaging 94(12):1211–1223

89. Kurhanewicz J, Vigneron DB, Hricak H, Narayan P, Carroll P, Nelson SJ (1996) Three-dimensional H-1 MR spectroscopic imaging of the in situ human prostate with high (0.24–0.7-cm^3) spatial resolution. Radiology 198(3):795–805

90. Zakian KL, Sircar K, Hricak H, Chen HN, Shukla-Dave A, Eberhardt S, Muruganandham M, Ebora L, Kattan MW, Reuter VE, Scardino PT, Koutcher JA (2005) Correlation of proton MR spectroscopic imaging with gleason score based on step-section pathologic analysis after radical prostatectomy. Radiology 234(3):804–814

91. Cai W, Zhu D, Byanju S, Chen J, Zhang H, Wang Y, Liao M (2019) Magnetic resonance spectroscopy imaging in diagnosis of suspicious prostate cancer: A meta-analysis. Medicine (Baltimore) 98(14):e14891

92. Starobinets O, Simko JP, Kuchinsky K, Kornak J, Carroll PR, Greene KL, Kurhanewicz J, Noworolski SM (2017) Characterization and stratification of prostate lesions based on comprehensive multiparametric MRI using detailed whole-mount histopathology as a reference standard. NMR Biomed 30(12):e3796

93. Steinseifer IK, van Asten JJ, Weiland E, Scheenen TW, Maas MC, Heerschap A (2015) Improved volume selective (1) H MR spectroscopic imaging of the prostate with gradient offset independent adiabaticity pulses at 3 tesla. Magn Reson Med 74(4):915–924

94. Gholizadeh N, Greer PB, Simpson J, Goodwin J, Fu C, Lau P, Siddique S, Heerschap A, Ramadan S (2021) Diagnosis of transition zone prostate cancer by multiparametric MRI: added value of MR spectroscopic imaging with sLASER volume selection. J Biomed Sci 28(1):54

95. Stamatelatou A, Scheenen TWJ, Heerschap A (2022) Developments in proton MR spectroscopic imaging of prostate cancer. MAGMA. https://doi.org/10.1007/s10334-022-01011-9

96. Kurhanewicz J, Vigneron DB, Ardenkjaer-Larsen JH, Bankson JA, Brindle K, Cunningham CH, Gallagher FA, Keshari KR, Kjaer A, Laustsen C, Mankoff DA, Merritt ME, Nelson SJ, Pauly JM, Lee P, Ronen S, Tyler DJ, Rajan SS, Spielman DM, Wald L, Zhang X, Malloy CR, Rizi R (2019) Hyperpolarized (13)C MRI: path to clinical translation in oncology. Neoplasia 21(1):1–16

97. Arteaga de Castro CS, van den Bergen B, Luijten PR, van der Heide UA, van Vulpen M, Klomp DW (2012) Improving SNR and B1 transmit field for an endorectal coil in 7 T MRI and MRS of prostate cancer. Magn Reson Med 68(1):311–318

98. Ardenkjaer-Larsen JH, Fridlund B, Gram A, Hansson G, Hansson L, Lerche MH, Servin R, Thaning M, Golman K (2003) Increase in signal-to-noise ratio of > 10,000 times in liquid-state NMR. Proc Natl Acad Sci U S A 100(18):10158–10163

99. Cunningham CH, Lau JY, Chen AP, Geraghty BJ, Perks WJ, Roifman I, Wright GA, Connelly KA (2016) Hyperpolarized 13C metabolic MRI of the human heart: initial experience. Circ Res 119(11):1177–1182

100. Sushentsev N, McLean MA, Warren AY, Benjamin AJV, Brodie C, Frary A, Gill AB, Jones J, Kaggie JD, Lamb BW, Locke MJ, Miller JL, Mills IG, Priest AN, Robb FJL, Shah N, Schulte RF, Graves MJ, Gnanapragasam VJ, Brindle KM, Barrett T, Gallagher FA (2022) Hyperpolarised (13)C-MRI identifies the emergence of a glycolytic cell population within intermediate-risk human prostate cancer. Nat Commun 13(1):466

101. Keshari KR, Sriram R, Van Criekinge M, Wilson DM, Wang ZJ, Vigneron DB, Peehl DM, Kurhanewicz J (2013) Metabolic reprogramming and validation of hyperpolarized 13C lactate as

a prostate cancer biomarker using a human prostate tissue slice culture bioreactor. Prostate 73(11):1171–1181

102. Day SE, Kettunen MI, Gallagher FA, Hu DE, Lerche M, Wolber J, Golman K, Ardenkjaer-Larsen JH, Brindle KM (2007) Detecting tumor response to treatment using hyperpolarized 13C magnetic resonance imaging and spectroscopy. Nat Med 13(11):1382–1387

103. Granlund KL, Tee SS, Vargas HA, Lyashchenko SK, Reznik E, Fine S, Laudone V, Eastham JA, Touijer KA, Reuter VE, Gonen M, Sosa RE, Nicholson D, Guo YW, Chen AP, Tropp J, Robb F, Hricak H, Keshari KR (2020) Hyperpolarized MRI of human prostate cancer reveals increased lactate with tumor grade driven by monocarboxylate transporter 1. Cell Metab 31 (1):105–114 e103.

104. Chatterjee A, Devaraj A, Mathew M, Szasz T, Antic T, Karczmar GS, Oto A (2019) Performance of T2 maps in the detection of prostate cancer. Acad Radiol 26(1):15–21

105. Chatterjee A, Nolan P, Sun C, Mathew M, Dwivedi D, Yousuf A, Antic T, Karczmar GS, Oto A (2020) Effect of echo times on prostate cancer detection on T2-weighted images. Acad Radiol 27(11):1555–1563

106. Mai J, Abubrig M, Lehmann T, Hilbert T, Weiland E, Grimm MO, Teichgraber U, Franiel T (2019) T2 Mapping in prostate cancer. Invest Radiol 54(3):146–152

107. Liu W, Turkbey B, Senegas J, Remmele S, Xu S, Kruecker J, Bernardo M, Wood BJ, Pinto PA, Choyke PL (2011) Accelerated T2 mapping for characterization of prostate cancer. Magn Reson Med 65(5):1400–1406

108. Gibbs P, Tozer DJ, Liney GP, Turnbull LW (2001) Comparison of quantitative T2 mapping and diffusion-weighted imaging in the normal and pathologic prostate. Magn Reson Med 46(6):1054–1058

109. Storas TH, Gjesdal KI, Gadmar OB, Geitung JT, Klow NE (2008) Prostate magnetic resonance imaging: multiexponential T2 decay in prostate tissue. J Magn Reson Imaging 28(5):1166–1172

110. Sabouri S, Chang SD, Savdie R, Zhang J, Jones EC, Goldenberg SL, Black PC, Kozlowski P (2017) Luminal water imaging: a new mr imaging T2 mapping technique for prostate cancer diagnosis. Radiology 284(2):451–459

111. Devine W, Giganti F, Johnston EW, Sidhu HS, Panagiotaki E, Punwani S, Alexander DC, Atkinson D (2019) Simplified luminal water imaging for the detection of prostate cancer from multiecho T2 MR images. J Magn Reson Imaging 50(3):910–917

112. Langer DL, van der Kwast TH, Evans AJ, Plotkin A, Trachtenberg J, Wilson BC, Haider MA (2010) Prostate tissue composition and MR measurements: investigating the relationships between ADC, T2, K(trans), v(e), and corresponding histologic features. Radiology 255(2):485–494

113. Chatterjee A, Bourne RM, Wang S, Devaraj A, Gallan AJ, Antic T, Karczmar GS, Oto A (2018) Diagnosis of prostate cancer with noninvasive estimation of prostate tissue composition by using hybrid multidimensional mr imaging: a feasibility study. Radiology 287(3):864–873

114. Wang S, Peng Y, Medved M, Yousuf AN, Ivancevic MK, Karademir I, Jiang Y, Antic T, Sammet S, Oto A, Karczmar GS (2014) Hybrid multidimensional T(2) and diffusion-weighted MRI for prostate cancer detection. J Magn Reson Imaging 39(4):781–788

115. Guivel-Scharen V, Sinnwell T, Wolff SD, Balaban RS (1998) Detection of proton chemical exchange between metabolites and water in biological tissues. J Magn Reson 133(1):36–45

116. Vinogradov E, Sherry AD, Lenkinski RE (2013) CEST: from basic principles to applications, challenges and opportunities. J Magn Reson 229:155–172

117. Zhou J, Payen JF, Wilson DA, Traystman RJ, van Zijl PC (2003) Using the amide proton signals of intracellular proteins and peptides to detect pH effects in MRI. Nat Med 9(8):1085–1090

118. Jia G, Abaza R, Williams JD, Zynger DL, Zhou J, Shah ZK, Patel M, Sammet S, Wei L, Bahnson RR, Knopp MV (2011) Amide proton transfer MR imaging of prostate cancer: a preliminary study. J Magn Reson Imaging 33(3):647–654

119. Takayama Y, Nishie A, Sugimoto M, Togao O, Asayama Y, Ishigami K, Ushijima Y, Okamoto D, Fujita N, Yokomizo A, Keupp J, Honda H (2016) Amide proton transfer (APT) magnetic resonance imaging of prostate cancer: comparison with Gleason scores. MAGMA 29(4):671–679

120. Yin H, Wang D, Yan R, Jin X, Hu Y, Zhai Z, Duan J, Zhang J, Wang K, Han D (2021) Comparison of diffusion kurtosis imaging and amide proton transfer imaging in the diagnosis and risk assessment of prostate cancer. Front Oncol 11:640906

121. Ma D, Gulani V, Seiberlich N, Liu K, Sunshine JL, Duerk JL, Griswold MA (2013) Magnetic resonance fingerprinting. Nature 495(7440):187–192

122. Hamilton JI, Jiang Y, Chen Y, Ma D, Lo WC, Griswold M, Seiberlich N (2017) MR fingerprinting for rapid quantification of myocardial T1, T2, and proton spin density. Magn Reson Med 77(4):1446–1458

123. Panda A, Obmann VC, Lo WC, Margevicius S, Jiang Y, Schluchter M, Patel IJ, Nakamoto D, Badve C, Griswold MA, Jaeger I, Ponsky LE, Gulani V (2019) MR fingerprinting and ADC mapping for characterization of lesions in the transition zone of the prostate gland. Radiology 292(3):685–694

124. Yu AC, Badve C, Ponsky LE, Pahwa S, Dastmalchian S, Rogers M, Jiang Y, Margevicius S, Schluchter M, Tabayoyong W, Abouassaly R, McGivney D, Griswold MA, Gulani V (2017) Development of a combined MR fingerprinting and diffusion examination for prostate cancer. Radiology 283(3):729–738

125. Zhang Y, Wells SA, Hernando D (2019) Stimulated echo based mapping (STEM) of T1, T2, and apparent diffusion coefficient: validation and protocol optimization. Magn Reson Med 81(1):167–181

126. Zhang Y, Wells SA, Triche BL, Kelcz F, Hernando D (2020) Stimulated-echo diffusion-weighted imaging with moderate b values for the detection of prostate cancer. Eur Radiol 30(6):3236–3244

127. Li M, Guo J, Hu P, Jiang H, Chen J, Hu J, Asbach P, Sack I, Li W (2021) Tomoelastography based on multifrequency MR elastography for prostate cancer detection: comparison with multiparametric MRI. Radiology 299(2):362–370

128. Li S, Chen M, Wang W, Zhao W, Wang J, Zhao X, Zhou C (2011) A feasibility study of MR elastography in the diagnosis of prostate cancer at 3.0T. Acta Radiol 52(3):354–358

129. Medved M, Newstead GM, Abe H, Zamora MA, Olopade OI, Karczmar GS (2006) High spectral and spatial resolution MRI of breast lesions: preliminary clinical experience. AJR Am J Roentgenol 186(1):30–37

130. Medved M, Chatterjee A, Devaraj A, Harmath C, Lee G, Yousuf A, Antic T, Oto A, Karczmar GS (2021) High spectral and spatial resolution MRI of prostate cancer: a pilot study. Magn Reson Med 86(3):1505–1513

131. Lagemaat MW, Philips BW, Vos EK, van Uden MJ, Futterer JJ, Jenniskens SF, Scheenen TW, Maas MC (2017) Feasibility of multiparametric magnetic resonance imaging of the prostate at 7 T. Invest Radiol 52(5):295–301

132. Nagayama M, Watanabe Y, Terai A, Araki T, Notohara K, Okumura A, Amoh Y, Ishimori T, Nakashita S, Dodo Y (2011) Determination of the cutoff level of apparent diffusion coefficient values for detection of prostate cancer. Jpn J Radiol 29(7):488–494

133. Metzger GJ, Kalavagunta C, Spilseth B, Bolan PJ, Li X, Hutter D, Nam JW, Johnson AD, Henriksen JC, Moench L, Konety B, Warlick CA, Schmechel SC, Koopmeiners JS (2016) Detection of prostate cancer: quantitative multiparametric MR imaging

models developed using registered correlative histopathology. Radiology 279(3):805–816

134. Meyer HJ, Wienke A, Surov A (2020) Discrimination between clinical significant and insignificant prostate cancer with apparent diffusion coefficient - a systematic review and meta analysis. BMC Cancer 20(1):482

135. Bajgiran AM, Mirak SA, Sung K, Sisk AE, Reiter RE, Raman SS (2019) Apparent diffusion coefficient (ADC) ratio versus conventional ADC for detecting clinically significant prostate cancer with 3-T MRI. AJR Am J Roentgenol 213(3):W134–W142

136. Donati OF, Mazaheri Y, Afaq A, Vargas HA, Zheng J, Moskowitz CS, Hricak H, Akin O (2014) Prostate cancer aggressiveness: assessment with whole-lesion histogram analysis of the apparent diffusion coefficient. Radiology 271(1):143–152

137. Haralick RM, Shanmugam K, Dinstein I (1973) Textural Features for Image Classification. IEEE Transactions on Systems, Man, and Cybernetics SMC-3, no. 6:610–621.

138. Galloway MM (1975) Texture analysis using gray level run lengths. Comput Graph Image Process 4:172–179

139. Dwivedi DK, Xi Y, Kapur P, Madhuranthakam AJ, Lewis MA, Udayakumar D, Rasmussen R, Yuan Q, Bagrodia A, Margulis V, Fulkerson M, Brugarolas J, Cadeddu JA, Pedrosa I (2021) Magnetic resonance imaging radiomics analyses for prediction of high-grade histology and necrosis in clear cell renal cell carcinoma: preliminary experience. Clin Genitourin Cancer 19 (1):12–21 e11.

140. Wibmer A, Hricak H, Gondo T, Matsumoto K, Veeraraghavan H, Fehr D, Zheng J, Goldman D, Moskowitz C, Fine SW, Reuter VE, Eastham J, Sala E, Vargas HA (2015) Haralick texture analysis of prostate MRI: utility for differentiating non-cancerous prostate from prostate cancer and differentiating prostate cancers with different Gleason scores. Eur Radiol 25(10):2840–2850

141. Stoyanova R, Takhar M, Tschudi Y, Ford JC, Solorzano G, Erho N, Balagurunathan Y, Punnen S, Davicioni E, Gillies RJ, Pollack A (2016) Prostate cancer radiomics and the promise of radiogenomics. Transl Cancer Res 5(4):432–447

142. Gillies RJ, Kinahan PE, Hricak H (2016) Radiomics: images are more than pictures. They Are Data Radiology 278(2):563–577

143. Udayakumar D, Zhang Z, Xi Y, Dwivedi DK, Fulkerson M, Haldeman S, McKenzie T, Yousuf Q, Joyce A, Hajibeigi A, Notgrass H, de Leon AD, Yuan Q, Lewis MA, Madhuranthakam AJ, Sibley RC, Elias R, Guo J, Christie A, McKay RM, Cadeddu JA, Bagrodia A, Margulis V, Brugarolas J, Wang T, Kapur P, Pedrosa I (2021) Deciphering intratumoral molecular heterogeneity in clear cell renal cell carcinoma with a radiogenomics platform. Clin Cancer Res 27(17):4794–4806

144. Montoya Perez I, Merisaari H, Jambor I, Ettala O, Taimen P, Knaapila J, Kekki H, Khan FL, Syrjala E, Steiner A, Syvanen KT, Verho J, Seppanen M, Rannikko A, Riikonen J, Mirtti T, Lamminen T, Saunavaara J, Falagario U, Martini A, Pahikkala T, Pettersson K, Bostrom PJ, Aronen HJ (2021) Detection of prostate cancer using biparametric prostate MRI, radiomics, and kallikreins: a retrospective multicenter study of men with a clinical suspicion of prostate cancer. J Magn Reson Imaging. https:// doi.org/10.1002/jmri.27811

145. Bi WL, Hosny A, Schabath MB, Giger ML, Birkbak NJ, Mehrtash A, Allison T, Arnaout O, Abbosh C, Dunn IF, Mak RH, Tamimi RM, Tempany CM, Swanton C, Hoffmann U, Schwartz LH, Gillies RJ, Huang RY, Aerts H (2019) Artificial intelligence in cancer imaging: Clinical challenges and applications. CA Cancer J Clin 69(2):127–157

146. Litjens G, Toth R, van de Ven W, Hoeks C, Kerkstra S, van Ginneken B, Vincent G, Guillard G, Birbeck N, Zhang J, Strand R, Malmberg F, Ou Y, Davatzikos C, Kirschner M, Jung F, Yuan J, Qiu W, Gao Q, Edwards PE, Maan B, van der Heijden F, Ghose S, Mitra J, Dowling J, Barratt D, Huisman H, Madabhushi A (2014) Evaluation of prostate segmentation algorithms for MRI: the PROMISE12 challenge. Med Image Anal 18(2):359–373

147. Tian Z, Liu L, Zhang Z, Fei B (2018) PSNet: prostate segmentation on MRI based on a convolutional neural network. J Med Imaging (Bellingham) 5(2):021208

148. Zhu Y, Wei R, Gao G, Ding L, Zhang X, Wang X, Zhang J (2019) Fully automatic segmentation on prostate MR images based on cascaded fully convolution network. J Magn Reson Imaging 49(4):1149–1156

149. Dai Z, Carver E, Liu C, Lee J, Feldman A, Zong W, Pantelic M, Elshaikh M, Wen N (2020) Segmentation of the prostatic gland and the intraprostatic lesions on multiparametric magnetic resonance imaging using mask region-based convolutional neural networks. Adv Radiat Oncol 5(3):473–481

150. Armato SG 3rd, Huisman H, Drukker K, Hadjiiski L, Kirby JS, Petrick N, Redmond G, Giger ML, Cha K, Mamonov A, Kalpathy-Cramer J, Farahani K (2018) PROSTATEx challenges for computerized classification of prostate lesions from multiparametric magnetic resonance images. J Med Imaging (Bellingham) 5(4):044501

151. Wang Z, Liu C, Cheng D, Wang L, Yang X, Cheng KT (2018) Automated detection of clinically significant prostate cancer in mp-MRI images based on an end-to-end deep neural network. IEEE Trans Med Imaging 37(5):1127–1139

152. Sushentsev N, Moreira Da Silva N, Yeung M, Barrett T, Sala E, Roberts M, Rundo L (2022) Comparative performance of fully-automated and semi-automated artificial intelligence methods for the detection of clinically significant prostate cancer on MRI: a systematic review. Insights Imaging 13(1):59

153. de Rooij M, Crienen S, Witjes JA, Barentsz JO, Rovers MM, Grutters JP (2014) Cost-effectiveness of magnetic resonance (MR) imaging and MR-guided targeted biopsy versus systematic transrectal ultrasound-guided biopsy in diagnosing prostate cancer: a modelling study from a health care perspective. Eur Urol 66(3):430–436

154. Cerci JJ, Fanti S, Lobato EE, Kunikowska J, Alonso O, Medina S, Novruzov F, Lengana T, Granados C, Kumar R, Rangarajan V, Al-Ibraheem A, Hourani M, Ali NS, Ahmad A, Keidar Z, Kucuk O, Elboga U, Bogoni M, Paez D (2022) Diagnostic performance and clinical impact of (68)Ga-PSMA-11 PET/CT imaging in early relapsed prostate cancer after radical therapy: a prospective multicenter study (IAEA-PSMA Study). J Nucl Med 63(2):240–247